

AT_1 fourth-order isogeometric phase-field modeling of brittle fracture

L. Greco, E. Maggiorcelli, M. Negri, A. Patton, A. Reali

Abstract. A crucial aspect in phase-field modeling, based on the variational formulation of brittle fracture, is the accurate representation of how the fracture surface energy is dissipated during the fracture process in the energy competition within a minimization problem. In general, the family of AT_1 functionals showcases a well-defined elastic limit and narrow transition regions before crack onset, as opposed to AT_2 models. On the other hand, high-order functionals provide similar accuracy as low-order ones but allow for larger mesh sizes in their discretization, remarkably reducing the computational cost. In this work, we aim to combine both these advantages and propose a novel AT_1 fourth-order phase-field model for brittle fracture within an isogeometric framework, which provides a straightforward discretization of the high-order term in the crack surface density functional. For the introduced AT_1 functional, we first prove a Γ -convergence result (in both the continuum and discretized isogeometric setting) based on a careful study of the optimal transition profile, which ultimately provides the explicit correction factor for the toughness and the exact size of the transition region. Fracture irreversibility is modeled by monotonicity of the damage variable and is conveniently enforced using the Projected Successive Over-Relaxation algorithm. Our numerical results indicate that the proposed fourth-order AT_1 model is more accurate than the considered lower-order AT_1 and AT_2 models; this allows to employ larger mesh sizes, entailing a lower computational cost.

AMS Subject Classification.

Introduction

Numerical simulation has the potential to serve as a decision-making tool in engineering, for example, at the design stage of structural elements of mechanical, civil, or aviation systems, ultimately reducing the reliance on expensive and time-consuming experimental tests to detect potential failure due to fracture. This requirement has led to developing many theoretical models and numerical methods.

The reference work on which fracture mechanics was founded is that of Griffith [20], based on the “competition” between stored elastic and dissipated fracture energy. More precisely, Griffith’s criterion asserts that fracture propagation occurs whenever the *energy release* G (the configurational variation of elastic energy with respect to the crack surface) reaches a critical value G_c (a material parameter, called *toughness*). In this approach, the physical crack is a (possibly branched) path in 2D or a surface in 3D. Alternatively, on the basis of [3], Bourdin et al. [6] introduced the phase-field approach for fracture: in this setting, the crack is represented by means of a scalar variable v taking values in $[0, 1]$, with $v = 1$ and $v = 0$ corresponding respectively to fracture and sound material. *Phase-field energies* usually take the form

$$\mathcal{F}_\varepsilon(\mathbf{u}, v) = \mathcal{E}_\varepsilon(\mathbf{u}, v) + G_c \mathcal{K}_\varepsilon(v),$$

where \mathbf{u} is the displacement, ε is the internal length, \mathcal{E}_ε is the elastic energy, while \mathcal{K}_ε is the crack surface energy. There are nowadays many choices for both \mathcal{K}_ε and \mathcal{E}_ε . For an extensive overview of phase-field work, we refer the interested reader to the following review works and books: [2, 30, 52, 7, 50].

In general, low-order energies take the form

$$\mathcal{K}_\varepsilon(v) = \int_\Omega (\varepsilon^{-1} \phi(v) + \varepsilon |\nabla v|^2) dx,$$

while their high-order counterparts [5, 24] read

$$\mathcal{K}_\varepsilon(v) = \int_\Omega (\varepsilon^{-1} \phi(v) + \varepsilon |\nabla v|^2 + \varepsilon^3 |\Delta v|^2) dx.$$

In the literature, the former are called second-order and the latter fourth-order; making reference to the associated Euler-Lagrange equations.

There are several choices for the function ϕ , see, e.g., [51] and the above references. Here, we mention only the most common: $\phi(v) = v$ and $\phi(v) = v^2$, corresponding to the so-called AT_1 and AT_2 functionals. From the mechanical point of view, AT_1 functionals have in general, better properties than AT_2 functionals since they result in a clear linear elastic regime before the onset of fracture. Indeed, as observed by Pham et al. [45], the linearity of ϕ introduces an analytical elastic limit of order $\sqrt{G_c\mu/\varepsilon}$ under which fracture does not occur. This consideration also makes this model interesting in the field of plasticity (see, e.g., Marengo et al. [39]). On the contrary, AT_2 promotes damage at arbitrarily small values of stress. Moreover, for given values of internal length and mesh size, the damage profile around the crack is usually narrower with AT_1 . It follows that numerical simulations carried out using the AT_1 model are closer to representing the physics behavior of the specimen and, therefore, a preferable modeling choice. Most often, simulations based on high-order functionals are more accurate approximating the dissipated energy, see, e.g., [19], and allow for larger mesh sizes, leading to considerably lower computational costs despite the extra effort related to second-order derivatives. As far as the elastic energy \mathcal{E}_ε , it is nowadays standard to employ energy splits to provide the correct mechanical behavior under tension, compression, and shear. Generally, elastic energies take the form

$$\mathcal{E}_\varepsilon(\mathbf{u}, v) = \int_{\Omega} (\psi_\varepsilon(v, \nabla v) W_+(\boldsymbol{\epsilon}) + W_-(\boldsymbol{\epsilon})) dx,$$

where ψ_ε is the degradation function and $\boldsymbol{\epsilon}$ is the strain. In the literature, there are actually several choices for both the terms W_\pm (e.g., volumetric-deviatoric [4], spectral [40], and the recent star-convex [49] decomposition) and the degradation function ψ_ε [51], with different mechanical outcomes, in particular under cyclic loadings.

The phase-field approach relies on the solid basis of Γ -convergence [14, 9] of the phase-field energy to the *sharp crack energy*, as the internal length ε vanishes. In this direction, besides [3], are nowadays available several interesting results, see e.g. [9, 12, 43, 11].

Evolutions are usually defined by means of time discrete incremental problems: at each time instant an *equilibrium configuration* of the system is computed, not necessarily being a global minimizer, subject to an irreversibility constraint. Numerically, different schemes are employed to find an equilibrium configuration, e.g., staggered [6], monolithic [16], and active set [23]. In this respect, note that the energy \mathcal{F}_ε is not (jointly) convex but only separately convex; therefore, in general, there are many equilibria and the solution to the incremental problem could be non-unique. Studying the time-continuous limit of the time-discrete evolutions [29, 28, 36, 37] reveals a peculiar feature of this model, actually shared by any rate-independent evolution for non-convex energies. There are two regimes of propagation: stable (or steady-state) and unstable (or catastrophic) [36, 37]. In the former, the evolution is continuous in time, and, noteworthy, it satisfies a phase-field version of Griffith's criterion. In the latter, a discontinuous instantaneous propagation occurs and Griffith's criterion is not always satisfied; in this case, dynamical or other rate-dependent models should be preferred.

In this work, we study a high-order AT_1 functional of the form $\mathcal{F}_\varepsilon(\mathbf{u}, v) = \mathcal{E}_\varepsilon(\mathbf{u}, v) + G_c \mathcal{K}_\varepsilon(v)$ (see §1). The elastic energy features the volumetric-deviatoric split [4]

$$\mathcal{E}_\varepsilon(\mathbf{u}, v) = \int_{\Omega} (\psi_\varepsilon(v) W_+(\boldsymbol{\epsilon}) + W_-(\boldsymbol{\epsilon})) dx, \quad W_+(\boldsymbol{\epsilon}) = \mu |\boldsymbol{\epsilon}_d|^2 + \kappa |\boldsymbol{\epsilon}_v^+|^2, \quad W_-(\boldsymbol{\epsilon}) = \kappa |\boldsymbol{\epsilon}_v^-|^2,$$

with a quadratic degradation function, i.e., $\psi_\varepsilon(v) = (v - 1)^2 + \eta_\varepsilon$ for $\eta_\varepsilon > 0$. The crack surface energy reads

$$\mathcal{K}_\varepsilon(v) = \frac{1}{c_\rho} \int_{\Omega} (\varepsilon^{-1} v + \varepsilon |\nabla v|^2 + \rho \varepsilon^3 |\Delta v|^2) dx,$$

where $\rho > 0$ is a parameter weighting the effects of the high-order term and c_ρ is the normalizing constant that depends on ρ . We underline that the present model is different from the one in [41], where a high-order AT_1 model is used to analyze anisotropy problems without considering the phase-field gradient term in the crack surface energy, as well as the technical tuning of c_ρ .

First of all, we provide a Γ -convergence result in §2. To this end, a main crucial point is the characterization of c_ρ (as a function of ρ) in such a way that the toughness is recovered exactly; in other terms, the factor c_ρ should be chosen in such a way that the sharp crack Γ -limit reads, in 2D,

$$\int_{\Omega \setminus J_u} W(\epsilon) dx + G_c \mathcal{H}^1(J_u),$$

where \mathcal{H}^1 is the 1-dimensional Hausdorff measure of the displacement jump J_u (loosely speaking, the length of the crack).

Technically, previous results in the literature, see, e.g., [9, 43, 11], do not apply here due to the combination of the high-order term and the constraint $v \in [0, 1]$. The value c_ρ is usually given by $c_\rho = 2\mathcal{K}(w_*)$, where w_* is the solution of the constrained optimal profile problem in \mathbb{R}_+ . However, this characterization is not useful for explicitly computing the optimal profile w_* . Hence, we developed a novel line of proof in §4 based on approximations with unconstrained local optimal profiles, which ultimately yield an explicit form for w_* . As a by product, we show that w_* is compactly supported in an interval $[0, R_*]$, where R_* is explicitly computed in terms of the coefficients of \mathcal{K}_ϵ . Note that, on the contrary, the optimal profile of AT_2 is an exponential, supported in the whole \mathbb{R}_+ . This technical point, has a couple of important benefits, for AT_1 versus AT_2 : the transition region is narrower and the value of toughness is better approximated. As a result, numerical simulations are very accurate at relatively large values of the internal length and mesh size.

After the mathematical part, the paper provides a detailed study of the numerical performance of the proposed AT_1 fourth-order model in §5. Dealing with high-order energies, we employ an isogeometric approach, as in, e.g., [5, 24, 19]. Isogeometric Analysis (IgA) was initially developed by Hughes et al. [25] to extend and enhance the capabilities of the finite element (FE) method in the field of geometric modeling, resulting in a technique also appearing to be preferable to standard FEs in many applications on the basis of per-degree-of-freedom accuracy. In particular, IgA displays a unique blend of features that can be harnessed for tackling challenges associated with the modeling of higher-order differential operators, among which higher-order accuracy, robustness, geometric flexibility, and, in particular, C^1 and higher-order continuity. The phase-field method in combination with an isogeometric discretization proved to be successful in studying fracture in a wide variety of problems involving, e.g., the modeling of structural elements in statics such as solid shells [1] and Kirchhoff-Love shells [48, 47], dynamics [32], but also different types of materials, e.g., piezoceramics [27], piezoelectric composites [26], porous functionally graded structures [44], and rock-like materials [31]. Furthermore, this technique has been applied within an IgA framework to the Cahn–Hilliard equation [21] and the isothermal Navier-Stokes–Korteweg equations [22] and extended to a wide variety of areas of science and engineering, including the modeling of shape memory alloys [15], liquid–vapor flows with surfactants [10], but also biomedical applications such as tumor growth [34, 35, 33], due to its capability to capture the interface implicitly without solving a moving boundary problem.

In this study, we consider various benchmarks to highlight different properties of the newly proposed AT_1 isogeometric higher-order model compared to with classical AT -models from the literature. For AT_1 , we link the mesh size h to the finite support of the optimal profile, i.e., to the value R_* , and just adopt the same choice of h for AT_2 (since R_* is not well defined). In this respect, it is important to remark that R_* actually depends on the coefficient ρ , appearing in the surface energy. In all numerical simulations, irreversibility is consistently enforced by applying the Projected Successive Over-Relaxation algorithm [38], which seamlessly integrates with the isogeometric discretization of the high-order functional under examination [19]. At first, we employ a pure tension setting to check the accuracy of the elastic limit. In this case, we compare only second- and fourth-order AT_1 functionals since AT_2 does not introduce a clear threshold for the stress before the onset of fracture. Our numerical results show that both functionals are extremely accurate, with a slightly better result for the fourth-order one. Next, we consider the Double Cantilever Beam (DCB) and the Single Edge Notch (SEN) tests under tension. In these Mode I benchmarks, the crack geometry is a straight line, which allows to focus on the accuracy of

the toughness. We compare fourth- and second-order AT_1 and AT_2 functionals. In essence, the fourth-order AT_1 functional performs better than the other AT -functionals, yielding very low errors on the toughness, at fixed mesh size, as well as higher convergence rates, with respect to the mesh size (see Table 3 and 4). Then, we consider a SEN under shear. In terms of toughness, the picture is very similar to that of the previous cases: the error is lower and the convergence rate higher. However, in terms of crack paths, fourth-order and second-order functionals produce quite different results (see Figure 10). We investigated this point in more detail in §6 by changing the weight ρ in front of the higher-order term in the surface integral. From this point of view, the picture is quite complex: for a fixed mesh size, smaller values of ρ are better in terms of elastic limit, while larger values are better in terms of toughness. Finally, in §7 we study the trade-off between accuracy and computational cost, and, more precisely, we investigate first the actual savings in terms of control points for a fixed level of accuracy and, then, the role of the mesh as R_* varies for different values of ρ . Finally, we draw our conclusions in §8.

1 Phase-field energy and governing equations

In this section, we introduce the phase-field energy and the evolution law in the time- and space-continuous setting.

1.1 Energy

The reference configuration Ω is an open, bounded, and Lipschitz domain in \mathbb{R}^2 . The set of admissible displacements is given by $\mathcal{U} = \{\mathbf{u} \in H^1(\Omega; \mathbb{R}^2) : \mathbf{u} = \mathbf{g} \text{ on } \partial_D \Omega\}$ where $\partial_D \Omega$ is a (relatively open) subset of the boundary $\partial \Omega$ and $\mathbf{g} \in W^{1,\infty}(\Omega; \mathbb{R}^2)$ is the boundary displacement at a given time. The phase-field density v belongs to the convex set $\mathcal{V} = H_{\text{div}}^1(\Omega; [0, 1]) = \{v \in H^1(\Omega) : v \in [0, 1], \Delta v \in L^2(\Omega)\}$. We consider the following AT_1 energy functional:

$$\mathcal{F}_\varepsilon(\mathbf{u}, v) = \mathcal{E}_\varepsilon(\mathbf{u}, v) + G_c \mathcal{K}_\varepsilon(v),$$

$$\mathcal{E}_\varepsilon(\mathbf{u}, v) = \int_\Omega W_\varepsilon(v, \boldsymbol{\epsilon}(\mathbf{u})) \, dx, \quad \mathcal{K}_\varepsilon(v) = \frac{1}{c_\rho} \int_\Omega (\varepsilon^{-1} v + \varepsilon |\nabla v|^2 + \rho \varepsilon^3 |\Delta v|^2) \, dx,$$

where $\boldsymbol{\epsilon}(\mathbf{u}) = \frac{1}{2}(\nabla \mathbf{u} + \nabla \mathbf{u}^T)$ is the linear strain, $\varepsilon > 0$ is the internal length, and $\rho > 0$ is a parameter. Clearly, for $\rho = 0$, the energy boils down to the lower order AT_1 functional (see Appendix A). The elastic energy density W_ε takes into account the volumetric-deviatoric split [4, 12] and is of the form

$$W(v, \boldsymbol{\epsilon}) := \psi_\varepsilon(v) W_+(\boldsymbol{\epsilon}) + W_-(\boldsymbol{\epsilon}), \quad W_+(\boldsymbol{\epsilon}) := \mu |\boldsymbol{\epsilon}_d|^2 + \kappa |\boldsymbol{\epsilon}_v^+|^2, \quad W_-(\boldsymbol{\epsilon}) := \kappa |\boldsymbol{\epsilon}_v^-|^2,$$

where $\psi_\varepsilon(v) = (v - 1)^2 + \eta_\varepsilon$ (for $\eta_\varepsilon > 0$) is the degradation function, $\boldsymbol{\epsilon}_v^+ := \frac{1}{2} \text{tr}^+(\boldsymbol{\epsilon}) \mathbf{I}$ and $\boldsymbol{\epsilon}_v^- := \frac{1}{2} \text{tr}^-(\boldsymbol{\epsilon}) \mathbf{I}$ are respectively the positive and negative volumetric parts of the strain, whereas $\boldsymbol{\epsilon}_d := \boldsymbol{\epsilon} - \boldsymbol{\epsilon}_v$ is its deviatoric part. The phase-field energy \mathcal{F}_ε provides an approximation of the sharp crack energy

$$\mathcal{F}(\mathbf{u}) = \int_{\Omega \setminus J_u} W(\boldsymbol{\epsilon}(\mathbf{u})) \, dx + G_c \mathcal{H}^1(J_u),$$

where the displacement \mathbf{u} belongs to the space $SBD^2(\Omega)$ and satisfies the non-interpenetration condition $[[\mathbf{u}]] \cdot \hat{\mathbf{n}} = (\mathbf{u}^+ - \mathbf{u}^-) \cdot \hat{\mathbf{n}} \geq 0$ on the crack set J_u .

In the sequel, we will prove that this convergence property holds in terms of Γ -convergence [9, 14] (as the internal length ε vanishes) at least in a reference one-dimensional case. Note that the scaling factor c_ρ in the energy \mathcal{F}_ε is needed to get the correct toughness value G_c in the limit energy \mathcal{F} . We will indeed provide an explicit formula for c_ρ , as a function of the parameter ρ .

1.2 Evolution law

We consider a quasi-static (rate-independent) evolution, driven by a boundary condition of the form $\mathbf{u} = t\mathbf{g}$ where $t \in [0, T]$ is a ‘‘pseudo-time’’ variable. As we consider linear elasticity, the energy at each time $t \in [0, T]$ can be written as $\mathcal{F}_\varepsilon(t, \mathbf{u}, v) = t^2 \mathcal{E}_\varepsilon(\mathbf{u}, v) + G_c \mathcal{K}_\varepsilon(v)$ for $\mathbf{u} \in \mathcal{U} = \{\mathbf{u} \in H^1(\Omega; \mathbb{R}^2) : \mathbf{u} = \mathbf{g} \text{ on } \partial_D \Omega\}$ and $v \in \mathcal{V}$. In the evolution we will further introduce the irreversibility constraint $\dot{v} \geq 0$.

It is well known that the energy \mathcal{F}_ε is only ‘‘separately convex’’ i.e., while $\mathcal{F}_\varepsilon(t, \mathbf{u}, \cdot) : \mathcal{V} \rightarrow [0, +\infty)$ and $\mathcal{F}_\varepsilon(t, \cdot, v) : \mathcal{U} \rightarrow [0, +\infty)$ are convex, the energy $\mathcal{F}_\varepsilon(t, \cdot, \cdot) : \mathcal{U} \times \mathcal{V} \rightarrow [0, +\infty)$ in general is not (jointly) convex. However, separate convexity is enough to characterize equilibrium configurations in terms of partial derivatives of the energy. More precisely, taking into account the irreversibility constraint, we will say that a configuration (\mathbf{u}, v) is in equilibrium at time $t \in [0, T]$ if

$$\partial_{\mathbf{u}} \mathcal{F}_\varepsilon(t, \mathbf{u}, v)[\boldsymbol{\xi}] = 0, \quad \partial_v \mathcal{F}_\varepsilon(t, \mathbf{u}, v)[\zeta] \geq 0$$

for every admissible variation $\boldsymbol{\xi} = \mathbf{w} - \mathbf{u}$ for $\mathbf{w} \in \mathcal{U}$ and $\zeta = z - v$ for $z \in \mathcal{V}$ with $z \geq v$; in other terms, by irreversibility the equilibrium of the phase-field is unilateral. The partial derivatives of the energy read

$$\begin{aligned} \partial_{\mathbf{u}} \mathcal{F}_\varepsilon(t, \mathbf{u}, v)[\boldsymbol{\xi}] &= \int_{\Omega} \partial_{\boldsymbol{\varepsilon}} W_\varepsilon(v, \boldsymbol{\varepsilon}(\mathbf{u})) : \boldsymbol{\varepsilon}(\boldsymbol{\xi}) \, dx, \\ \partial_v \mathcal{F}_\varepsilon(t, \mathbf{u}, v)[\zeta] &= \int_{\Omega} \partial_v W_\varepsilon(v, \boldsymbol{\varepsilon}(\mathbf{u})) \zeta \, dx + \frac{G_c}{c_\rho} \int_{\Omega} (\varepsilon^{-1} \zeta - 2\varepsilon \nabla v \cdot \nabla \zeta + 2\rho \varepsilon^3 \Delta v \Delta \zeta) \, dx. \end{aligned}$$

Note that $\partial_{\boldsymbol{\varepsilon}} W_\varepsilon(v, \boldsymbol{\varepsilon}(\mathbf{u}))$ gives the phase-field stress $\boldsymbol{\sigma}(v, \mathbf{u}) = 2\psi_\varepsilon(v)(\mu \boldsymbol{\varepsilon}_d(\mathbf{u}) + \kappa \boldsymbol{\varepsilon}_v^+(\mathbf{u})) - 2\kappa \boldsymbol{\varepsilon}_v^-(\mathbf{u})$, while $\partial_v W_\varepsilon(v, \boldsymbol{\varepsilon}(\mathbf{u}))$ gives the crack driving force.

Since the energy \mathcal{F}_ε is non-convex, in the quasi-static setting, we should expect both stable (or steady-state) and unstable (or catastrophic) propagation regimes, see, e.g., [36]. For the sake of simplicity, we confine ourselves to the former since the latter is delicate and should be better governed by dynamics or other rate-dependent effects. In the quasi-static setting, the stable regime is governed by the following system:

$$\begin{cases} \partial_{\mathbf{u}} \mathcal{F}_\varepsilon(t, \mathbf{u}(t), v(t))[\boldsymbol{\xi}] = 0 \\ \partial_v \mathcal{F}_\varepsilon(t, \mathbf{u}(t), v(t))[\zeta] \geq 0, \quad \partial_v \mathcal{F}_\varepsilon(t, \mathbf{u}(t), v(t))[\dot{v}(t)] = 0, \quad \dot{v}(t) \geq 0, \end{cases} \quad (1)$$

where $\boldsymbol{\xi} = \mathbf{w} - \mathbf{u}(t)$ for $\mathbf{w} \in \mathcal{U}$ and $\zeta = z - v(t)$ for $z \in \mathcal{V}$ with $z \geq v(t)$.

In practice this evolution is obtained by solving incremental problems in a time-discrete setting. Let us consider the discrete times $t_k = kT/n_{ts}$ where n_{ts} is the number of time steps and $k = 0, \dots, n_{ts}$. Starting from an equilibrium configuration $(\mathbf{u}(t_{k-1}), v(t_{k-1}))$ at time t_{k-1} we employ the staggered scheme

$$\begin{cases} \mathbf{u}_{m+1} \in \operatorname{argmin}\{\mathcal{F}(t_k, \mathbf{u}, v_m) : \mathbf{u} \in \mathcal{U}\} \\ v_{m+1} \in \operatorname{argmin}\{\mathcal{F}(t_k, \mathbf{u}_m, v) : v \in \mathcal{V}, v \geq v(t_{k-1})\} \end{cases}$$

to provide (technically, up to subsequences) an equilibrium configuration $(\mathbf{u}(t_k), v(t_k))$ which satisfies the discrete counterpart of (1), i.e.,

$$\begin{cases} \partial_{\mathbf{u}} \mathcal{F}(t, \mathbf{u}(t_k), v(t_k))[\boldsymbol{\xi}] = 0 \\ \partial_v \mathcal{F}(t, \mathbf{u}(t_k), v(t_k))[\zeta] \geq 0, \quad \partial_v \mathcal{F}(t, \mathbf{u}(t_k), v(t_k))[v(t_k) - v(t_{k-1})] = 0, \quad v(t_k) \geq v(t_{k-1}). \end{cases}$$

Here, we do not enter into the mathematical details about these evolutions. For second-order functionals, we refer the reader to [37] for a comprehensive analysis of (1) including Griffith’s criterion in the phase-field context.

2 Statement of the Γ -convergence result

2.1 One-dimensional setting

For the sake of simplicity, let us consider an interval (a, b) . Let $\mathcal{U} = H^1(a, b)$ be the space of admissible displacements and $\mathcal{V} = H^2((a, b); [0, 1])$ the set of admissible phase-field functions. For $\varepsilon > 0$ and $\eta_\varepsilon = o(\varepsilon)$, let $\mathcal{F}_\varepsilon : L^1(a, b) \times L^1(a, b) \rightarrow [0, +\infty]$ be the AT_1 functional defined by

$$\mathcal{F}_\varepsilon(u, v) = \begin{cases} \int_{(a,b)} (\kappa\psi_\varepsilon(v)|u'_+|^2 + \kappa|u'_-|^2) dx + \frac{G_c}{c_\rho} \int_{(a,b)} (\varepsilon^{-1}v + \varepsilon|v'|^2 + \rho\varepsilon^3|v''|^2) dx & (u, v) \in \mathcal{U} \times \mathcal{V}, \\ +\infty & \text{otherwise,} \end{cases} \quad (2)$$

with $\psi_\varepsilon(v) = (v - 1)^2 + \eta_\varepsilon$. In the sequel, we will provide the explicit value of c_ρ (as a function of ρ), while the parameter $\rho > 0$ will be of the form $1/\gamma^2$ (this choice will be convenient to compute c_ρ in §3.3). In order to simplify the notation, we omit the dependence of the energy on the parameter ρ . In §4, we will prove the convergence of (2) to the functional $\mathcal{F} : L^1(a, b) \times L^1(a, b) \rightarrow [0, +\infty]$ defined as follows:

$$\mathcal{F}(u, v) = \begin{cases} \int_{(a,b) \setminus J_u} \kappa|u'|^2 dx + G_c \# J_u & \text{if } u \in SBV^2(a, b) \text{ with } \llbracket u \rrbracket > 0 \text{ and } v = 0 \text{ a.e. in } (a, b), \\ +\infty & \text{otherwise.} \end{cases} \quad (3)$$

Note that the energy \mathcal{F} is finite if $u' \in L^2(a, b)$, the number of discontinuities is finite, and the non-interpenetration condition $\llbracket u \rrbracket > 0$ is satisfied in the jump points. The optimality constant c_ρ will be characterized in §3.

Before stating our main convergence result, it is necessary to define the *optimal profile problem*, which will ultimately provide the constant c_ρ for the Γ -convergence result. First, let us introduce the transition energy with unit internal length, $\mathcal{K} : \mathcal{W} \rightarrow \mathbb{R}$ given by

$$\mathcal{K}(w) := \int_{\mathbb{R}_+} (w + |w'|^2 + \gamma^{-2}|w''|^2) dx,$$

where $\mathcal{W} = \{w \in L^1(\mathbb{R}_+) : w' \in H^1(\mathbb{R}_+), w(0) = 1, w'(0) = 0\}$. We now provide a result of existence and uniqueness of the optimal profile that will be subsequently characterized in §3.

Proposition 2.1. *There exists a unique*

$$w_* \in \operatorname{argmin} \{\mathcal{K}(w) : w \in \mathcal{W} \text{ such that } 0 \leq w \leq 1\}. \quad (4)$$

Proof. Take the *minimizing sequence* $\{\hat{w}_n\}_{n \in \mathbb{N}} \subset \mathcal{W}$ such that $\mathcal{K}(\hat{w}_n) \rightarrow \inf\{\mathcal{K}(w) : w \in \mathcal{W} \text{ such that } 0 \leq w \leq 1\}$. Observe that such a sequence $\{\hat{w}_n\}_{n \in \mathbb{N}}$ is bounded in $H^2(\mathbb{R}_+)$. Indeed, being $0 \leq w_n \leq 1$, $\|w_n\|_{H^2(\mathbb{R}_+)}^2 = \int_{\mathbb{R}_+} (|w_n|^2 + |w'_n|^2 + |w''_n|^2) dx \leq C \int_{\mathbb{R}_+} (|w_n| + |w'_n|^2 + \gamma^{-2}|w''_n|^2) dx < +\infty$ by definition of \mathcal{W} . Therefore, it exists a (non-relabelled) subsequence of $\{\hat{w}_n\}_{n \in \mathbb{N}}$ that weakly converges in $H^2(\mathbb{R}_+)$ to a certain $w_* \in H^2(\mathbb{R}_+)$. The set $\{w \in \mathcal{W} : 0 \leq w \leq 1\}$ is weakly closed (being convex and strongly closed) in $H^2(\mathbb{R}_+)$, whence w_* belongs to this set. Now, since the functional \mathcal{K} is weakly-lower semicontinuous (being strictly convex), we obtain that w_* is indeed the unique minimum in definition (4). ■

In §4 we will prove the following Γ -convergence result.

Theorem 2.2. *Let $c_\rho = 2\mathcal{K}(w_*)$ and let $\eta_\varepsilon = o(\varepsilon)$. Then, \mathcal{F}_ε Γ -converges to \mathcal{F} as $\varepsilon \rightarrow 0^+$ with respect to the (strong) topology of $L^1(a, b) \times L^1(a, b)$.*

For numerical purposes it is fundamental to know the support of the optimal profile w_* (in order to calibrate the mesh size) and the explicit value of the constant c_ρ (to estimate the effective toughness). To this purpose, in §3 we will prove the following result.

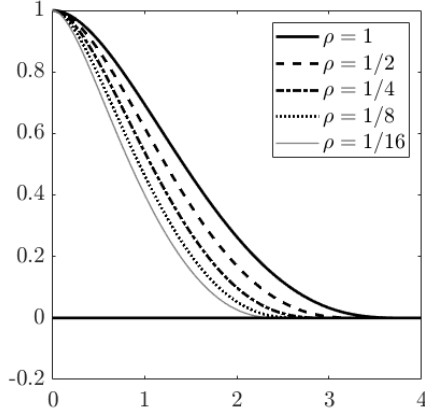


Figure 1: The optimal profiles w_* as a function of ρ .

Theorem 2.3. *The support of w_* is the finite interval $[0, R_*]$ where R_* is the unique solution of the non-linear equation*

$$\gamma R_*(1 + \cosh(\gamma R_*)) = 2(\gamma + 1) \sinh(\gamma R_*). \quad (5)$$

In the interval $[0, R_]$ the optimal profile takes the form*

$$w_*(x) = a_3(r_*)(\cosh(\gamma x) - 1) + a_4(r_*)(\sinh(\gamma x) - \gamma x) + \frac{1}{4}x^2 + 1, \quad (6)$$

where $r_ = \gamma R_*$ while a_3 and a_4 are given in (15) and (16). The optimal constant c_ρ takes the form*

$$c_\rho = \frac{2(1 + \gamma)}{\gamma R_*} + \frac{(1 + 2\gamma)R_*}{2\gamma} - \frac{R_*^3}{24}. \quad (7)$$

Remark 2.4. *As the optimal profile w_* has compact support, it turns out that the phase-field “interfaces” of AT_1 are narrower than those of AT_2 ; indeed the optimal profile of AT_2 is supported in the whole \mathbb{R}_+ (see, for instance, [43]). Moreover, the support of w_* increases with $\rho = 1/\gamma^2$ (see Figure 1).*

In our numerical simulations, the weight $\rho = 1/\gamma^2$ appearing in the phase-field energy \mathcal{F}_ε takes values of the form 2^i for $i \in \{-4, \dots, 4\}$. From (5), by a fixed point algorithm, we obtain (with arbitrary precision) the explicit values of R_* from which we can compute c_ρ from (7). Such values, as a function of $\rho = 1/\gamma^2$, are reported in Table 1.

Table 1: Tabulated c_ρ and R_* values for $\rho = \{\frac{1}{16}, \frac{1}{8}, \frac{1}{4}, \frac{1}{2}, 1, 2, 4, 8, 16\}$.

ρ	$\frac{1}{16}$	$\frac{1}{8}$	$\frac{1}{4}$	$\frac{1}{2}$	1	2	4	8	16
R_*	2.4998	2.7045	2.9847	3.3554	3.8300	4.4230	5.1515	6.0387	7.1265
c_ρ	3.1615	3.3593	3.6281	3.9852	4.4485	5.0369	5.7715	6.6714	7.7022

2.2 Isogeometric setting

In this section, we provide the statement of the Γ -convergence result in the isogeometric setting. Consider a (physical) mesh \mathcal{T}_h of size h in the interval $[a, b]$ and let $\mathcal{S}_h \subset H^2(a, b)$ be the space of splines on \mathcal{T}_h . We denote by $\mathcal{U}_h = \mathcal{S}_h$ the space for the displacement and by \mathcal{V}_h the set for the phase field, i.e., $\mathcal{V}_h = \{v_h \in \mathcal{S}_h : v_h \in [0, 1]\}$. As $\mathcal{S}_h \subset H^2(a, b)$, the isogeometric functional $\mathcal{F}_{\varepsilon, h}$ is simply the restriction of the functional \mathcal{F}_ε to the spline spaces \mathcal{S}_h . More precisely, $\mathcal{F}_{\varepsilon, h} : L^1(a, b) \times L^1(a, b) \rightarrow [0, +\infty]$ is given

by

$$\mathcal{F}_{\varepsilon,h}(u_h, v_h) = \int_{(a,b)} (\kappa \psi_\varepsilon(v_h) |u'_h|_+^2 + \kappa |u'_h|_-^2) dx + \frac{G_c}{c_\rho} \int_{(a,b)} (\varepsilon^{-1} v_h + \varepsilon |v'_h|^2 + \rho \varepsilon^3 |v''_h|^2) dx, \quad (8)$$

for $(u_h, v_h) \in \mathcal{U}_h \times \mathcal{V}_h$ and $\mathcal{F}_{\varepsilon,h}(u_h, v_h) = +\infty$ otherwise. The convergence result is stated in the next Theorem.

Theorem 2.5. *Let $c_\rho = 2\mathcal{K}(w_*)$, $\eta_\varepsilon = o(\varepsilon)$, and $h = o(\varepsilon)$, then $\mathcal{F}_{\varepsilon,h}$ Γ -converges to \mathcal{F} as $\varepsilon \rightarrow 0^+$ with respect to the (strong) topology of $L^1(a, b) \times L^1(a, b)$.*

We do not enter into the technical details and do not provide a proof, which follows from Theorem 2.2 together with the arguments of [43]. However, we highlight that the mesh size h is much smaller than the internal length ε ; this is fundamental in order to obtain the correct Γ -limit and, in particular, the right value of toughness, choosing h of order ε would result in a case similar to that of [42], where the toughness depends on the orientation of the mesh.

3 Optimal profile: characterization of w_* and c_ρ

3.1 Auxiliary unconstrained problems

Let us now introduce the localized energies with unit internal length, $\mathcal{K}_R : \mathcal{W}_R \rightarrow \mathbb{R}$ given by

$$\mathcal{K}_R(w) := \int_{(0,R)} (w + |w'|^2 + \gamma^{-2} |w''|^2) dx,$$

where $\mathcal{W}_R = \{w \in H^2(0, R) : w(0) = 1, w'(0) = 0, w(R) = 0, w'(R) = 0\}$. Let us now consider the minimization problem

$$w_R \in \operatorname{argmin} \{\mathcal{K}_R(w) : w \in \mathcal{W}_R\}. \quad (9)$$

We remark on the fact that, in contrast to (4), in (9), it is not required that $0 \leq w \leq 1$. In general, solutions w_R do not satisfy the constraint $0 \leq w_R \leq 1$ (see Figure 2). However, solutions taking values in $[0, 1]$ will be fundamental to characterize the optimal profile and will be called *admissible solutions*; indeed, we will see that the support of the optimal profile w_* is the finite interval $[0, R_*]$, where $R_* = \max\{R > 0 : 0 \leq w_R \leq 1\}$.

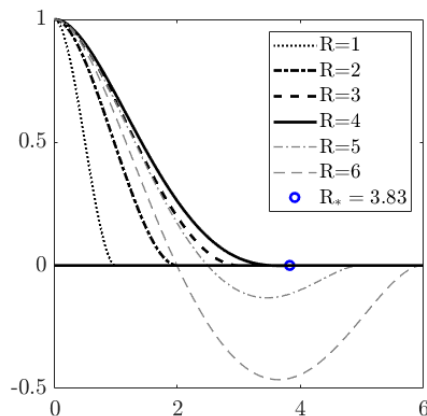


Figure 2: Solutions w_R of (9) as a function of R for fixed $\rho = 1$ and the value R_* corresponding to the maximum strictly positive value of the interval limit such that the profile $0 \leq w_R \leq 1$ (namely, $0 \leq w_R \leq 1$ for $R \leq R_*$, while w_R takes negative values for $R > R_*$).

Arguing as in Proposition 2.1, it follows that the minimizer in (9) is unique; moreover, it is characterized by

$$\begin{cases} 1 - 2w_R'' + \frac{2}{\gamma^2}w_R^{(4)} = 0 & \text{on } (0, R) \\ w_R(0) = 1 \\ w_R'(0) = 0 \\ w_R(R) = 0 \\ w_R'(R) = 0. \end{cases} \quad (10)$$

The solution of this ODE has the form

$$w_R(x) = b_1 + b_2x + b_3 \cosh(\gamma x) + b_4 \sinh(\gamma x) + \frac{1}{4}x^2. \quad (11)$$

Indeed $\frac{1}{4}x^2$ is a particular solution while the characteristic polynomial of the associated homogeneous equation has roots $\lambda_{1,2} = 0$ with multiplicity two and $\lambda_{3,4} = \pm\gamma$ (an explicit calculation of the coefficients b_i is provided in the sequel).

3.2 Characterization of w_*

The next propositions establish the link between the (global constrained) profile w_* and the local unconstrained profiles w_R introduced in §3.1.

Proposition 3.1. *It exists $R_* > 0$ such that the support of w_* is $[0, R_*]$ (the value of R_* will be characterized in Proposition 3.5). Moreover, $w_*|_{[0, R_*]}(x) = w_{R_*}(x)$, where w_{R_*} is the unique solution of (10) with $R = R_*$.*

Proof. Notice that $w_*(x) < 1$ for all $x > 0$. Indeed, if it existed $R' > 0$ such that $w_*(R') = 1$, then $w_*'(R') = 0$ (R' is a maximum point, since $0 \leq w_* \leq 1$, and, by Sobolev embedding, w_* is of class C^1), hence $\hat{w}(x) := w_*(x + R')$ is an admissible competitor for w_* , indeed it belongs to \mathcal{W} , and satisfies $0 \leq \hat{w} \leq 1$. On the other hand, $\mathcal{K}(\hat{w}) < \mathcal{K}(w_*)$, which is in contradiction with (4).

We define $R_* := \inf\{x : w_*(x) = 0\}$ and observe that $R_* < +\infty$. Indeed, if this was not the case, $0 < w_*(x) < 1$ for all $x \in \mathbb{R}_+$ and thus $d\mathcal{K}(w_*)[\xi] = 0$ for all $\xi \in C_0^\infty(\mathbb{R}_+)$, that means w_* is the solution of:

$$\begin{cases} 1 - 2w'' + \frac{2}{\gamma^2}w^{(4)} = 0 & \text{on } (0, +\infty) \\ w(0) = 1 \\ w'(0) = 0. \end{cases} \quad (12)$$

The solution of this ODE has the form $w(x) = b_1 + b_2x + b_3 \cosh(\gamma x) + b_4 \sinh(\gamma x) + \frac{1}{4}x^2$. Such a function does not belong to $L^1(\mathbb{R}_+)$ for any choice of the coefficients b_i (as in any case it tends either to $+\infty$ or $-\infty$ for $x \rightarrow +\infty$), which is in contradiction with (4).

Note that $w_*|_{[R_*, +\infty)} = 0$, indeed, being $w_*(R_*) = 0$ and $0 \leq w_* \leq 1$, R_* is a minimum point for w_* and thus $w_*'(R_*) = 0$. As a consequence, the function

$$\bar{w}(x) = \begin{cases} w_*(x) & x < R_* \\ 0 & x \geq R_* \end{cases}$$

belongs to the space \mathcal{W} and satisfies $0 \leq \bar{w} \leq 1$. Hence, by minimality it coincides with the unique minimizer w_* of \mathcal{K} . We have hence proven the first part of the proposition.

Now, the function $w_*|_{(0, R_*)}$ takes values in $(0, 1)$, hence $d\mathcal{K}(w_*)[\xi] = 0$ for every $\xi \in C_0^\infty(0, R)$; therefore, it solves

$$\begin{cases} 1 - 2w'' + \frac{2}{\gamma^2}w^{(4)} = 0 & \text{on } (0, R_*) \\ w(0) = 1 \\ w'(0) = 0 \\ w(R_*) = 0 \\ w'(R_*) = 0 \end{cases} \quad (13)$$

where the last condition comes from the fact that R_* is a minimum point. Hence, $w_*|_{[0, R_*]}(x) = w_{R_*}(x)$, where w_{R_*} is the unique solution of (9) for $R = R_*$. ■

Proposition 3.2. *It holds that $R_* = \max\{R \in (0, +\infty) : w_R \in [0, 1]\}$.*

Proof. As proven in Proposition 3.1, the function w_* solves (13) and by definition takes values in $(0, 1)$. Therefore, R_* belongs to the set $\{R \in (0, +\infty) : w_R \in [0, 1]\}$; hence, the latter set is non-empty and $R_* \leq \sup\{R \in (0, +\infty) : w_R \in [0, 1]\}$.

To prove the inverse inequality, assume by contradiction that there exists $\bar{R} > R_*$ such that $0 \leq w_{\bar{R}} \leq 1$. By definition $w_{\bar{R}}$ minimizes $\mathcal{K}_{\bar{R}}$ over the set $\mathcal{W}_{\bar{R}}$ and it takes values in $[0, 1]$, so

$$w_{\bar{R}} \in \operatorname{argmin} \{\mathcal{K}_{\bar{R}}(w) : w \in \mathcal{W}_{\bar{R}} \text{ such that } w \in [0, 1]\}.$$

Now, by Proposition 3.1, $w_*|_{[R_*, +\infty)} = 0$ and $w'_*(R_*) = 0$; from this, since $R_* < \bar{R}$, it follows that $w_*(\bar{R}) = w'_*(\bar{R}) = 0$. Therefore, by definition (4) of w_* , it holds that

$$w_*|_{[0, \bar{R}]} \in \operatorname{argmin} \{\mathcal{K}_{\bar{R}}(w) : w \in \mathcal{W}_{\bar{R}} \text{ such that } w \in [0, 1]\}.$$

By uniqueness of the minimizer, $w_*|_{[0, \bar{R}]}(x) = w_{\bar{R}}(x)$. This is a contradiction, since $w_*(x) = 0$ for $x > R_*$ while $w_{\bar{R}}(x)$ has the form (11) with $R = \bar{R}$. ■

Remark 3.3. In Propositions 3.1 and 3.2, it was shown that the solution of (4) is precisely given by the *admissible solution* w_R with the largest possible support.

3.3 Computation of R_* and c_ρ

In this section, we will provide several explicit calculations and, to this end, it is convenient to consider first the *general auxiliary problem* of finding z_r such that:

$$\begin{cases} 1 - 2\gamma^2 z_r'' + 2\gamma^2 z_r^{(4)} = 0 & \text{on } (0, r) \\ z_r(0) = 1 \\ z_r'(0) = 0 \\ z_r(r) = 0 \\ z_r'(r) = 0. \end{cases} \quad (14)$$

The solution of the ODE (14) has the form

$$z_r(y) = a_1(r) + a_2(r)y + a_3(r) \cosh(y) + a_4(r) \sinh(y) + \frac{y^2}{4\gamma^2}.$$

Indeed $y^2/4\gamma^2$ is a particular solution, while the characteristic polynomial of the associated homogeneous equation has roots $\lambda_{1,2} = 0$ with multiplicity two and $\lambda_{3,4} = \pm 1$. Thus, the boundary conditions read:

$$\begin{cases} a_1(r) + a_3(r) = 1 \\ a_2(r) + a_4(r) = 0 \\ a_1(r) + a_2(r)r + a_3(r) \cosh(r) + a_4(r) \sinh(r) + \frac{r^2}{4\gamma^2} = 0 \\ a_2(r) + a_3(r) \sinh(r) + a_4(r) \cosh(r) + \frac{r}{2\gamma^2} = 0, \end{cases}$$

that can be rewritten as the linear system $\mathbf{Ax} = \mathbf{b}$, with:

$$\mathbf{A} = \begin{pmatrix} \cosh(r) - 1 & \sinh(r) - r \\ \sinh(r) & \cosh(r) - 1 \end{pmatrix}, \quad \mathbf{x} = \begin{pmatrix} a_3(r) \\ a_4(r) \end{pmatrix}, \quad \mathbf{b} = - \begin{pmatrix} 1 + \frac{r^2}{4\gamma^2} \\ \frac{r}{2\gamma^2} \end{pmatrix}$$

together with the conditions $a_1(r) = 1 - a_3(r)$ and $a_2(r) = -a_4(r)$. From direct calculations it follows that:

$$a_3(r) = \frac{(A_{22}b_1 - A_{12}b_2)}{\det(A)} = -\frac{(r^2 + 4\gamma^2)\cosh(r) + r^2 - 4\gamma^2 - 2r\sinh(r)}{4\gamma^2(2 - 2\cosh(r) + r\sinh(r))} = 1 - a_1(r), \quad (15)$$

$$a_4(r) = \frac{(-A_{21}b_1 + A_{11}b_2)}{\det(A)} = \frac{(r^2 + 4\gamma^2)\sinh(r) + 2r - 2r\cosh(r)}{4\gamma^2(2 - 2\cosh(r) + r\sinh(r))} = -a_2(r). \quad (16)$$

Given these coefficients, we can write z_r in the following condensed form:

$$z_r(y) = a_3(r)(\cosh(y) - 1) + a_4(r)(\sinh(y) - y) + \frac{y^2}{4\gamma^2} + 1. \quad (17)$$

Clearly, the function z_r is the unique minimizer of the energy

$$\mathcal{J}_r(z) := \int_{(0,r)} (z + \gamma^2|z'|^2 + \gamma^2|z''|^2) dy \quad (18)$$

over the set $\mathcal{Z}_r = \{z \in H^2(0, r) : z(0) = 1, z'(0) = 0, z(r) = 0, z'(r) = 0\}$. Finally, note that in general z_r does not satisfy the admissibility constraint $z_r \in [0, 1]$; however, solutions with $z_r \in [0, 1]$ will play an important role in the characterization of the optimal profile.

Remark 3.4. Setting $r = \gamma R$, by a simple change of variable, we get $w_R(x) = z_r(\gamma x)$, where z_r is the unique solution of (14), from which we also get an explicit expression for w_R :

$$w_R(x) = z_r(\gamma x) = a_3(r)(\cosh(\gamma x) - 1) + a_4(r)(\sinh(\gamma x) - \gamma x) + \frac{1}{4}x^2 + 1. \quad (19)$$

Moreover, it turns out that $R_* = \frac{r_*}{\gamma}$ where $r_* = \sup\{r \in (0, +\infty) : z_r \in [0, 1]\}$.

Proposition 3.5. *The value of r_* is characterized by the non-linear equation $z_{r_*}''(r_*) = 0$, from which it follows the expression:*

$$r_* = \frac{2(\gamma + 1)\sinh(r_*)}{1 + \cosh(r_*)}. \quad (20)$$

Proof. We claim that for any fixed $r > 0$, if $z_r \geq 0$ then $z_r \leq 1$. Indeed, if this was not the case, $\hat{y} = \operatorname{argmax}\{z_r(y) : y \in (0, r)\}$ would be such that $z_r(\hat{y}) > 1$. The function

$$\hat{z}(y) := \begin{cases} \frac{z_r(y+\hat{y})}{z_r(\hat{y})} & y \in [0, r - \hat{y}] \\ 0 & x \in [r - \hat{y}, r] \end{cases}$$

is such that $\hat{z} \in \mathcal{Z}_r$ and $\mathcal{J}_r(\hat{z}) < \mathcal{J}_r(z_r)$, which is a contradiction since z_r is the unique minimizer of \mathcal{J}_r over \mathcal{Z}_r . Therefore, the admissible solutions z_r of (14), i.e., those such that $z_r \in [0, 1]$, must only satisfy the constraint $z_r \geq 0$ (since, as just observed, the condition $z_r \leq 1$ follows *for free* by minimality). As a consequence, $r_* = \sup\{r \in (0, +\infty) : z_r \geq 0\}$.

In the following, we will examine the values of $r > 0$ for which the admissibility condition $z_r \geq 0$ is met. Firstly, let us prove that the condition $z_r''(r) \geq 0$ is necessary to guarantee that $z_r \geq 0$. If $r > 0$ is such that $z_r''(r) < 0$, then it exists $y < r$ sufficiently close to r such that $z_r(y) < 0$. Indeed, by continuity, $z_r''(y) < 0$ for y sufficiently close to r and, being $z_r'(r) = 0$, z_r is increasing near r and thus $z_r(y) < z_r(r) = 0$. Therefore, for such $r > 0$, z_r is not admissible.

On the other hand, we claim that $z_r''(r) > 0$ implies $z_r \geq 0$, and we prove it by contradiction. If this was not the case, $z_r(r') < 0$ where $r' := \operatorname{argmin}\{z_r(y) : y \in (0, r)\}$. We set $r'' := \max\{y : z_r(y) > 0, z_r'(y) = 0\}$ and observe that $r' < r'' < r$; indeed, by the same reasoning as before, $z_r''(r) > 0$ implies $z_r > 0$ in a left neighborhood of r . Now, $z_r|_{(r', r)}$ is the unique solution of

$$\begin{cases} 1 - 2\gamma^2 z'' + 2\gamma^2 z^{(4)} = 0 & \text{on } (r', r) \\ z(r') = z_r(r') \\ z'(r') = 0 \\ z(r) = 0 \\ z'(r) = 0. \end{cases} \quad (21)$$

We denote

$$\mathcal{J}_{(r',r)}(z) = \int_{(r',r)} (z + \gamma^2|z'|^2 + \gamma^2|z''|^2) dy$$

and observe that $z_r|_{(r',r)}$ is the unique minimizer of $\mathcal{J}_{(r',r)}$ over the set $\{z \in H^2(r',r) : z(r') = z_r(r'), z'(r') = z(r) = z'(r) = 0\}$. We define

$$z_\alpha(y) := \begin{cases} z_r(r') + \beta_\alpha(z_r(y) - z_r(r')) & y \in (r', r'') \\ \alpha z_r(y) & y \in (r'', r) \end{cases}$$

for any $\alpha \in (0, 1)$ and set $\beta_\alpha = \frac{\alpha z_r(r'') - z_r(r')}{z_r(r'') - z_r(r')} \in (0, 1)$ so as to have continuity of z_α . We remark that our choice of r' and r'' guarantees that $z_\alpha(y) < z_r(y)$. Indeed, for all $x \in (r', r'')$, by definition of r' , $z_r(y) > z_r(r')$ and therefore $z_\alpha(y) = z_r(r') + \beta_\alpha(z_r(y) - z_r(r')) < z_r(r') + (z_r(y) - z_r(r')) = z_r(y)$. Moreover, $z_r > 0$ in a left neighborhood of r , $z_r|_{[r'',r]} \geq 0$, ensuring that $\alpha z_r(y) < z_r(y)$ on (r'', r) . Now,

$$z'_\alpha(y) = \begin{cases} \beta_\alpha z'_r(y) & y \in (r', r'') \\ \alpha z'_r(y) & y \in (r'', r) \end{cases}$$

and, being r'' a stationary point, $z'_\alpha(r''_-) = z'_\alpha(r''_+) = 0$. It follows that $z'_\alpha \in H^1(r', r)$ and its weak derivative is

$$z''_\alpha(y) = \begin{cases} \beta_\alpha z''_r(y) & y \in (r', r'') \\ \alpha z''_r(y) & y \in (r'', r). \end{cases}$$

Consequently, being $z_\alpha \leq z_r$ and $\alpha, \beta_\alpha \in (0, 1)$, we get $\mathcal{J}_{(r',r)}(z_\alpha) < \mathcal{J}_{(r',r)}(z_r|_{(r',r)})$, which is in contradiction with the minimality of z_r .

Summarizing what has just been proven, if $z''_r(r) > 0$ then z_r is admissible, while if $z''_r(r) < 0$ then z_r is not admissible. Therefore, in order to characterize the admissible values of $r > 0$, one has to study the sign of

$$z''_r(r) = -\frac{r^2(1 + \cosh(r) - 4r \sinh(r) + 4(\gamma^2 - 1)(1 - \cosh(r)))}{4\gamma^2(2 - 2 \cosh(r) + r \sinh(r))}. \quad (22)$$

Equation (22) is obtained by substituting the explicit expressions (15) and (16) of $a_i(r)$ in $z''_r(r) = a_3(r) \cosh(r) + a_4(r) \sinh(r) + \frac{1}{2\gamma^2}$, as follows:

$$\begin{aligned} z''_r(r) &= \frac{1}{4\gamma^2(2 - 2 \cosh(r) + r \sinh(r))} \left(-(r^2 + 4\gamma^2) \cosh^2(r) - r^2 \cosh(r) + 4\gamma^2 \cosh(r) + 2r \sinh(r) \cosh(r) \right. \\ &\quad \left. + (r^2 + 4\gamma^2) \sinh^2(r) + 2r \sinh(r) - 2r \cosh(r) \sinh(r) + 2(2 - 2 \cosh(r) + r \sinh(r)) \right) \\ &= \frac{-(r^2 + 4\gamma^2) - r^2 \cosh(r) + 4\gamma^2 \cosh(r) + 4r \sinh(r) + 4 - 4 \cosh(r)}{4\gamma^2(2 - 2 \cosh(r) + r \sinh(r))} \\ &= -\frac{r^2(1 + \cosh(r)) - 4r \sinh(r) + 4(\gamma^2 - 1)(1 - \cosh(r))}{4\gamma^2(2 - 2 \cosh(r) + r \sinh(r))}. \end{aligned}$$

For $r > 0$, the denominator in (22) is always positive: indeed, by direct calculations, as $r \rightarrow 0$, $F(r) := \frac{2(\cosh(r)-1)}{\sinh(r)}$ goes to zero with unit slope, while $F''(r) := \frac{-2(\cosh(r)-1)^2}{\sinh^3(r)}$ is always negative and hence $r > \frac{2(\cosh(r)-1)}{\sinh(r)}$. Thereby, to study the sign of $z''_r(r)$, it is sufficient to look for the roots of the numerator (as a quadratic polynomial in r), that are the fixed points of

$$G_{1,2}(r) := \frac{2(1 \pm \gamma) \sinh(r)}{1 + \cosh(r)}. \quad (23)$$

Observe that it does not exist $r > 0$ such that $r = G_2(r) = \frac{2(1-\gamma) \sinh(r)}{1+\cosh(r)}$: if $\gamma > 1$, then $G_2(r) < 0 < r$, while if $\gamma < 1$, then G_2 is strictly concave (in fact $G'_2(r) = \frac{2(1-\gamma)}{1+\cosh(r)}$ is decreasing) and, as $r \rightarrow 0$, it goes

to zero with slope equal to $1 - \gamma$, which is smaller than 1, the slope of r . So, $G_2(r) < r$ for all $r > 0$. On the other hand, the positive fixed point of $G_1(r) = \frac{2(1+\gamma)\sinh(r)}{1+\cosh(r)}$ is unique. In fact, G_1 is strictly concave (as before, $G_1'(r) = \frac{2(1+\gamma)}{1+\cosh(r)}$ is decreasing) and as $r \rightarrow 0$, it goes to zero with slope equal to $1 + \gamma$, which is greater than 1, the slope of r . Therefore, the only admissible values of r are those in between 0 and the positive fixed point of G_1 , denoted by r_* . \blacksquare

Remark 3.6. Since the local profiles w_R are defined in terms of z_r by (19), the natural condition $w_R \leq 1$ is not actually needed in the optimal profile problem (9) since it follows *for free* by minimality, as highlighted in the proof of Proposition 3.5. Moreover, the admissibility condition $w_R \geq 0$ is equivalent to the condition $w_R''(R) \geq 0$.

Proposition 3.7. *The solution of (4) is $w_*(x) := z_{r_*}(\gamma x)$ where*

$$z_{r_*}(y) = \begin{cases} -\frac{2\gamma+1}{2\gamma^2}(\cosh(y) - 1) + \left(\frac{r_*}{4\gamma^2} + \frac{1+\gamma}{\gamma r_*}\right)(\sinh(y) - y) + \frac{y^2}{4\gamma^2} + 1 & [0, r_*] \\ 0 & (r_*, +\infty). \end{cases} \quad (24)$$

Proof. Rearranging (15), we obtain that

$$\begin{aligned} a_3(r) &= \frac{2\gamma^2 - 2\gamma^2 \cosh(r) + r \sinh(r)}{2\gamma^2(2 - 2\cosh(r) + r \sinh(r))} - \frac{r^2(\cosh(r) + 1)}{4\gamma^2(2 - 2\cosh(r) + r \sinh(r))} \\ a_4(r) &= \frac{r}{4\gamma^2} + \frac{\sinh(r)}{2 - 2\cosh(r) + r \sinh(r)}. \end{aligned} \quad (25)$$

Substituting $r = r_* = \frac{2(\gamma+1)\sinh(r_*)}{1+\cosh(r_*)}$ from (20), we get:

$$\begin{aligned} a_3(r_*) &= \frac{2\gamma^2 - 2\gamma^2 \cosh(r_*) + \frac{2(1+\gamma)\sinh^2(r_*)}{1+\cosh(r_*)}}{2\gamma^2\left(2 - 2\cosh(r_*) + \frac{2(1+\gamma)\sinh^2(r_*)}{1+\cosh(r_*)}\right)} - \frac{\frac{4(1+\gamma)^2\sinh^2(r_*)}{1+\cosh(r_*)}}{4\gamma^2\left(2 - 2\cosh(r_*) + \frac{2(1+\gamma)\sinh^2(r_*)}{1+\cosh(r_*)}\right)} \\ &= \frac{2(\gamma^2 - \gamma^2 \cosh^2(r_*) + (1+\gamma)\sinh^2(r_*))}{4\gamma^2(1 - \cosh^2(r_*) + (1+\gamma)\sinh^2(r_*))} - \frac{(1+\gamma)^2\sinh^2(r_*)}{2\gamma^2(1 - \cosh^2(r_*) + (1+\gamma)\sinh^2(r_*))} \\ &= \frac{-\gamma^2 + \gamma + 1}{2\gamma^3} - \frac{(1+\gamma)^2}{2\gamma^3} = -\frac{2\gamma + 1}{2\gamma^2}; \\ a_4(r_*) &= \frac{r_*}{4\gamma^2} + \frac{\sinh(r_*)}{2 - 2\cosh(r_*) + \frac{2(1+\gamma)\sinh^2(r_*)}{1+\cosh(r_*)}} = \frac{r_*}{4\gamma^2} + \frac{\sinh(r_*)(1 + \cosh(r_*))}{2(1 - \cosh^2(r_*) + (1+\gamma)\sinh^2(r_*))} \\ &= \frac{r_*}{4\gamma^2} + \frac{1 + \cosh(r_*)}{2\gamma \sinh(r_*)} = \frac{r_*}{4\gamma^2} + \frac{1 + \gamma}{\gamma r_*}. \end{aligned}$$

The thesis immediately follows from (17). \blacksquare

Lemma 3.8. *The function $w_*(x) = z_{r_*}(\gamma x)$ is such that:*

$$\mathcal{K}(w_*) = \frac{1}{2\gamma} \int_{(0, r_*)} z_{r_*}(s) ds + \gamma z_{r_*}'''(0). \quad (26)$$

As a consequence, the optimal constant is given by the explicit expression

$$c_\rho = \frac{2(1+\gamma)}{r_*} + \frac{(1+2\gamma)r_*}{2\gamma^2} - \frac{r_*^3}{24\gamma^3},$$

or equivalently by (7).

Proof. By definition and by a simple change of variable,

$$\begin{aligned}
\mathcal{K}(w_*) &= \int_{\mathbb{R}_+} \left(w_* + |w_*'|^2 + \frac{1}{\gamma^2} |w_*''|^2 \right) dx = \frac{1}{\gamma} \int_{(0, r_*)} (z_{r_*} + \gamma^2 |z_{r_*}'|^2 + \gamma^2 |z_{r_*}''|^2) dy \\
&= \frac{1}{\gamma} \left(\int_{(0, r_*)} \left(\left(\frac{1}{2} + \frac{1}{2} \right) z_{r_*} - \gamma^2 z_{r_*}'' z_{r_*} + \gamma^2 z_{r_*}^{(4)} z_{r_*} \right) dy + \gamma^2 z_{r_*}'''(0) \right) \\
&= \frac{1}{\gamma} \int_{(0, r_*)} \left(\frac{1}{2} z_{r_*} + \frac{1}{2} (1 - 2\gamma^2 z_{r_*}'' + 2\gamma^2 z_{r_*}^{(4)}) z_{r_*} \right) dy + \gamma z_{r_*}'''(0) = \frac{1}{2\gamma} \int_{(0, r_*)} z_{r_*} dy + \gamma z_{r_*}'''(0),
\end{aligned}$$

where the third equality comes from integration by parts. Last equality simply follows from the fact that, since z_r solves (14), the terms in parentheses have zero sum.

Now, in order to obtain the optimal constant c_ρ , which is defined as $c_\rho = 2\mathcal{K}(w_*)$, it is sufficient to substitute the explicit expression of z_{r_*} , given in Proposition 3.7, into (26). In detail, we start by computing:

$$z_{r_*}'''(0) = a_3(r_*) \sinh(0) + a_4(r_*) \cosh(0) = a_4(r_*).$$

Subsequently, we calculate:

$$\int_{(0, r_*)} z_{r_*} dy = a_3(r_*) (\sinh(r_*) - r_*) + a_4(r_*) \left(\cosh(r_*) - 1 - \frac{r_*^2}{2} \right) + \frac{r_*^3}{12\gamma^2} + r_*.$$

According to (26), adding these terms to $2\gamma^2 z_{r_*}'''(0) = 2\gamma^2 a_4(r_*)$ and, using equation (20), one obtains the following expression for $2\gamma\mathcal{K}(w_*)$:

$$\begin{aligned}
2\gamma\mathcal{K}(w_*) &= \int_{\mathbb{R}_+} z_{r_*} dy + 2\gamma^2 a_4(r_*) = a_3(r_*) (\sinh(r_*) - r_*) + a_4(r_*) \left(\cosh(r_*) - 1 - \frac{r_*^2}{2} + 2\gamma^2 \right) + \frac{r_*^3}{12\gamma^2} + r_* \\
&= a_3(r_*) \sinh(r_*) + \left(\frac{r_*}{4\gamma^2} + \frac{1+\gamma}{\gamma r_*} \right) \left((\cosh(r_*) + 1) + 2(\gamma^2 - 1) - \frac{r_*^2}{2} \right) + \frac{r_*^3}{12\gamma^2} + r_* (1 - a_3(r_*)) \\
&= -\frac{(2\gamma + 1) \sinh(r_*)}{2\gamma^2} + \left(\frac{(\gamma + 1) \sinh(r_*)}{2\gamma^2 (1 + \cosh(r_*))} + \frac{1 + \cosh(r_*)}{2\gamma \sinh(r_*)} \right) (\cosh(r_*) + 1) \\
&\quad + \left(\frac{r_*}{4\gamma^2} + \frac{1+\gamma}{\gamma r_*} \right) \left(2(\gamma^2 - 1) - \frac{r_*^2}{2} \right) + \frac{r_*^3}{12\gamma^2} + r_* (1 - a_3(r_*)) \\
&= -\frac{(2\gamma + 1) \sinh(r_*)}{2\gamma^2} + \frac{(\gamma + 1) \sinh(r_*)}{2\gamma^2} + \frac{(1 + \cosh(r_*))^2}{2\gamma \sinh(r_*)} + \frac{r_* (\gamma^2 - 1)}{2\gamma^2} + \frac{2(\gamma^2 - 1)(1 + \gamma)}{\gamma r_*} \\
&\quad - \frac{r_*^3}{8\gamma^2} - \frac{r_* (1 + \gamma)}{2\gamma} + \frac{r_*^3}{12\gamma^2} + r_* (1 - a_3(r_*)) \\
&= \frac{-\sinh^2(r_*) + 1 + \cosh^2(r_*) + 2 \cosh(r_*)}{2\gamma \sinh(r_*)} + \frac{2(\gamma^2 - 1)(1 + \gamma)}{\gamma r_*} \\
&\quad + r_* \left(\frac{\gamma^2 - 1}{2\gamma^2} - \frac{1 + \gamma}{2\gamma} + 1 + \frac{2\gamma + 1}{2\gamma^2} \right) - \frac{r_*^3}{24\gamma^2} \\
&= \frac{1 + \cosh(r_*)}{\gamma \sinh(r_*)} + \frac{2(\gamma^2 - 1)(1 + \gamma)}{\gamma r_*} + r_* \frac{2\gamma + 1}{2\gamma} - \frac{r_*^3}{24\gamma^2} \\
&= \frac{2(1 + \gamma)}{\gamma r_*} + \frac{2(\gamma^2 - 1)(1 + \gamma)}{\gamma r_*} + r_* \frac{2\gamma + 1}{2\gamma} - \frac{r_*^3}{24\gamma^2} \\
&= \frac{2(1 + \gamma)\gamma}{r_*} + r_* \frac{2\gamma + 1}{2\gamma} - \frac{r_*^3}{24\gamma^2}.
\end{aligned}$$

Therefore, the optimal constant is given by:

$$c_\rho = 2\mathcal{K}(w_*) = \frac{2(1 + \gamma)}{r_*} + r_* \frac{2\gamma + 1}{2\gamma^2} - \frac{r_*^3}{24\gamma^3}$$

and the proof is concluded. ■

4 Proof of the Γ -convergence result

For $\varepsilon_n \rightarrow 0^+$ we employ the notation $\mathcal{F}_n = \mathcal{F}_{\varepsilon_n}$ and $\psi_n = \psi_{\varepsilon_n}$.

4.1 Liminf inequality

Lemma 4.1. *Let $(u_n, v_n) \rightarrow (u, v)$ in $L^1(a, b) \times L^1(a, b)$ such that $\liminf_{n \rightarrow +\infty} \mathcal{F}_n(u_n, v_n) < +\infty$ then $u \in SBV^2(a, b)$ with $\llbracket u \rrbracket > 0$, $v = 0$ a.e. in (a, b) and*

$$c_\rho \# J_u \leq \liminf_{n \rightarrow +\infty} \int_{(a,b)} (\varepsilon_n^{-1} v_n + \varepsilon_n |v_n'|^2 + \rho \varepsilon_n^3 |v_n''|^2) dx, \quad (27)$$

$$\int_{(a,b) \setminus J_u} |u'|^2 dx \leq \liminf_{n \rightarrow +\infty} \int_{(a,b)} (\psi_n(v_n) |u_n'|_+^2 + |u_n'|_-^2) dx. \quad (28)$$

Proof. I. Clearly, it is enough to consider the case when the liminf in (27)-(28) are finite. Upon extracting a subsequence (non relabeled) it is not restrictive to assume that the liminf in (27) and (28) is actually a limit. Thus, $u_n \in \mathcal{U} = H^1(a, b)$ and $v_n \in \mathcal{V} = H^2(a, b; [0, 1])$ for every $n \in \mathbb{N}$. In particular, $v_n \geq 0$ and

$$\int_{(a,b)} (\varepsilon_n^{-1} |v_n| + \varepsilon_n |v_n'|^2) dx \leq \int_{(a,b)} (\varepsilon_n^{-1} v_n + \varepsilon_n |v_n'|^2 + \rho \varepsilon_n^3 |v_n''|^2) dx.$$

It follows that

$$\mathcal{H}_n(u_n, v_n) = \int_{(a,b)} \psi_n(v_n) |u_n'|^2 dx + \int_{(a,b)} (\varepsilon_n^{-1} |v_n| + \varepsilon_n |v_n'|^2) dx \leq C \mathcal{F}_n(u_n, v_n) \leq C'.$$

The functional \mathcal{H}_n introduced above is a (classical second order) elliptic approximation of the Mumford-Shah functional; therefore, we can employ the compactness arguments of [9, Theorem 3.15] from which it follows that $u \in SBV^2(a, b)$, $v = 0$ a.e. on (a, b) , and that $u_n \rightharpoonup u$ in $H^1((a, b) \setminus J_u^\delta)$ for every $\delta > 0$, where $J_u^\delta = \{x : \text{dist}(J_u, x) \leq \delta\}$.

Let us check that $\llbracket u \rrbracket > 0$. Assume by contradiction that $\llbracket u(s) \rrbracket < 0$ for some $s \in J_u$, i.e., $u^+(s) < u^-(s)$. Let $\eta = \frac{1}{4} |\llbracket u \rrbracket|$. For every $\delta > 0$ (sufficiently small) there exist $s - \delta < s' < s'' < s + \delta$ such that $u_n(s') \rightarrow u(s') > u^-(s) - \eta$ and $u_n(s'') \rightarrow u(s'') < u^+(s) + \eta$. If $n \gg 1$ it turns out that

$$\int_{(s', s'')} |u_n'|_- dx \geq |u_n(s'') - u_n(s')| = u_n(s') - u_n(s'') \geq u^-(s) - u^+(s) - 2\eta \geq \frac{1}{2} |\llbracket u(s) \rrbracket|.$$

Hence, by Jensen's inequality and by the boundedness of the energies

$$\frac{1}{4} |\llbracket u(s) \rrbracket|^2 \leq \left(\int_{(s', s'')} |u_n'|_- dx \right)^2 \leq (s'' - s') \int_{(s', s'')} |u_n'|_-^2 dx \leq 2\delta C.$$

By the arbitrariness of δ it follows that $|\llbracket u(s) \rrbracket| = 0$.

II. In order to prove (27) we “localize” around jump points. Let $J_u = \{s_i : i = 1, \dots, N\}$ and let $0 < \delta \ll 1$ such that the intervals $J_i^\delta = [s_i - \delta, s_i + \delta]$ are disjoint and contained in (a, b) . Clearly

$$\int_{(a,b)} (\varepsilon^{-1} v_n + \varepsilon |v_n'|^2 + \rho \varepsilon^3 |v_n''|^2) dx \geq \sum_{i=1}^N \int_{J_i^\delta} (\varepsilon^{-1} v_n + \varepsilon |v_n'|^2 + \rho \varepsilon^3 |v_n''|^2) dx,$$

and thus it is enough to prove that for every $i = 1, \dots, N$ it holds

$$\liminf_{n \rightarrow +\infty} \int_{J_i^\delta} (\varepsilon^{-1} v_n + \varepsilon |v_n'|^2 + \rho \varepsilon^3 |v_n''|^2) dx \geq c_\rho. \quad (29)$$

We follow the outline of [43, Proposition 4.1]. Upon extracting a subsequence (not relabelled) it is not restrictive to assume that $v_n \rightarrow 0$ a.e. in $(-\delta, \delta)$. Moreover, for simplicity of notation we assume that the interval J_i^δ is of the form $[-\delta, \delta]$, i.e. that $0 \in J_u$.

We claim that there exists $\hat{x}_n \in (-\delta, \delta)$ with $\hat{x}_n \rightarrow 0$ such that $v_n(\hat{x}_n) \rightarrow 1^-$ and $v'_n(\hat{x}_n) = 0$. Let $\delta' > 0$ (sufficiently small) such that $v_n(-\delta') \rightarrow 0$ and $v_n(\delta') \rightarrow 0$. Let $x_n \in \operatorname{argmax}\{v_n(x) : x \in [-\delta', \delta']\}$. Let us check that $\lim_{n \rightarrow +\infty} v_n(x_n) = 1$. Assume by contradiction that there exists a subsequence (non relabeled) such that $\max\{v_n(x) : x \in [-\delta', \delta']\} \leq C < 1$. Then $\psi_n(v_n(x)) > C' > 0$ for every $x \in [-\delta', \delta']$ and thus

$$\mathcal{F}_n(u_n, v_n) \geq C' \int_{(-\delta', \delta')} |u'_n|^2 dx.$$

Hence, $\{u_n\}$ is bounded in $H^1(-\delta', \delta')$ and its limit u belongs to $H^1(-\delta', \delta')$, which contradicts $0 \in J_u$. As $v_n(-\delta') \rightarrow 0$ and $v_n(\delta') \rightarrow 0$ the maximizer x_n actually belongs to the open interval $(-\delta', \delta')$ and thus $v'_n(x_n) = 0$. The claim follows by the arbitrariness of δ' .

For simplicity, let us assume that $\hat{x}_n = 0$ and define the rescaled functions $w_n(s) = v_n(\varepsilon_n s)$ for $|s| \leq R_n = \delta/\varepsilon_n$. Then, by a change of variable,

$$\int_{J_i^\delta} (\varepsilon_n^{-1} v_n + \varepsilon_n |v'_n|^2 + \rho \varepsilon_n^3 |v''_n|^2) dx = \int_{(-R_n, R_n)} (w_n + |w'_n|^2 + \rho |w''_n|^2) dx.$$

Note that $w_n(0) \rightarrow 1^-$ and $w'_n(0) = 0$. Clearly, for $n \gg 1$ and every $M \in \mathbb{N}$ we have

$$\int_{(0, M)} (w_n + |w'_n|^2 + \rho |w''_n|^2) dx \leq C$$

and thus w_n is a bounded sequence in $H^2(0, M)$. By a diagonal argument it follows that there exists a subsequence (non relabelled) and a function $w \in H^2_{loc}(0, +\infty)$ such that $w_n \rightharpoonup w$ in $H^2(0, M)$ for every $M \in \mathbb{N}$. As a consequence

$$\begin{aligned} \liminf_{n \rightarrow +\infty} \int_{(0, R_n)} (w_n + |w'_n|^2 + \rho |w''_n|^2) dx &\geq \liminf_{n \rightarrow +\infty} \int_{(0, M)} (w_n + |w'_n|^2 + \rho |w''_n|^2) dx \\ &\geq \int_{(0, M)} (w + |w'|^2 + \rho |w''|^2) dx. \end{aligned}$$

Taking the supremum with respect to M yields

$$\liminf_{n \rightarrow +\infty} \int_{(0, R_n)} (w_n + |w'_n|^2 + \rho |w''_n|^2) dx \geq \int_{(0, +\infty)} (w + |w'|^2 + \rho |w''|^2) dx = \mathcal{K}(w) \geq \mathcal{K}(w_*).$$

Arguing in the same way in the interval $(-\infty, 0)$ we finally get (29), since $c_\rho = 2\mathcal{K}(w_*)$.

III. It remains to prove (28). First, note that $\psi_n(v_n) - \eta_n = (v_n - 1)^2 \rightarrow 1$ strongly in $L^2(a, b)$ (for instance by dominated convergence) and remember that $u_n \rightharpoonup u$ in $H^1((a, b) \setminus J_u^\delta)$ for every $\delta > 0$. As a consequence $(\psi_n(v_n) - \eta_n)^{1/2} u'_n \rightharpoonup u'$ in $L^2((a, b) \setminus J_u^\delta)$ for every $\delta > 0$ (by weak-strong convergence). Therefore,

$$\liminf_{n \rightarrow +\infty} \int_{(a, b) \setminus J_u^\delta} (\psi_n(v_n) |u'_n|_+^2 + |u'_n|_-^2) dx \geq \liminf_{n \rightarrow +\infty} \int_{(a, b) \setminus J_u^\delta} (\psi_n(v_n) - \eta_n) |u'_n|^2 dx \geq \int_{(a, b) \setminus J_u^\delta} |u'|^2 dx.$$

Taking the supremum with respect to $\delta > 0$ yields (28). \blacksquare

From Lemma 4.2 and by a standard supremum of measures argument [9, Proposition 1.16] the following Γ -liminf estimate holds.

Lemma 4.2. *Let $(u_n, v_n) \rightarrow (u, v)$ in $L^1(a, b) \times L^1(a, b)$ such that $\liminf_{n \rightarrow +\infty} \mathcal{F}_n(u_n, v_n) < +\infty$ then $u \in SBV^2(a, b)$ with $\llbracket u \rrbracket > 0$, $v = 0$ a.e. in (a, b) , and*

$$\int_{(a, b) \setminus J_u} \kappa |u'|^2 dx + G_c \# J_u \leq \liminf_{n \rightarrow +\infty} \mathcal{F}_n(u_n, v_n).$$

4.2 Limsup inequality

Proposition 4.3. *Let $u \in SBV^2(a, b)$ with $\llbracket u \rrbracket > 0$. There exist $u_n \in \mathcal{U} = H^1(a, b)$ and $v_n \in \mathcal{V} = H^2(a, b; [0, 1])$ such that $u_n \rightarrow u$ in $L^1(a, b)$, $v_n \rightarrow 0$ in $L^1(a, b)$ and*

$$\int_{(a,b)} (\psi_n(v_n) |u'_n|_+^2 + |u'_n|_-^2) dx \rightarrow \int_{(a,b) \setminus J_u} |u'|^2 dx, \quad (30)$$

$$\int_{(a,b)} (\varepsilon_n^{-1} v_n^2 + \varepsilon_n |v'_n|^2 + \rho \varepsilon_n^3 |v''_n|^2) dx \rightarrow c_\rho \# J_u. \quad (31)$$

Proof. It is not restrictive to consider the case of a single crack, i.e., $J_u = \{s\}$. Let $\eta_n \ll \delta_n \ll \varepsilon_n$. As $\llbracket u \rrbracket > 0$ for $n \gg 1$ we have $u(s + \delta_n) > u(s - \delta_n)$. Let us define the functions

$$u_n(x) = \begin{cases} u(x) & \text{for } x < s - \delta_n \\ tu(s + \delta_n) + (1-t)u(s - \delta_n) & \text{for } s - \delta_n \leq x \leq s + \delta_n \text{ and } t = (x - s + \delta_n)/2\delta_n \\ u(x) & \text{for } x > s + \delta_n, \end{cases}$$

$$v_n(x) = \begin{cases} w_*((s - \delta_n - x)/\varepsilon_n) & \text{for } x < s - \delta_n \\ 1 & \text{for } s - \delta_n \leq x \leq s + \delta_n \\ w_*((x - s - \delta_n)/\varepsilon_n) & \text{for } x > s + \delta_n. \end{cases}$$

Note that $u_n \in H^1(a, b)$ and that $u'_n > 0$ in $(s - \delta_n, s + \delta_n)$. Note also that $v_n \in H^2(a, b)$ since $v_n(0) = 1$ and $v'_n(0) = 0$ and that $\text{supp}(v_n) \subset (s - \delta_n - \varepsilon_n R_*, s + \delta_n + \varepsilon_n R_*)$. It is easy to check that $u_n \rightarrow u$ in $L^1(a, b)$ and $v_n \rightarrow 0$ in $L^1(a, b)$. Let us write

$$\int_{(a,b)} (\psi_n(v_n) |u'_n|_+^2 + |u'_n|_-^2) dx = \int_{(a, s - \delta_n)} (\psi_n(v_n) |u'_n|_+^2 + |u'_n|_-^2) dx + \int_{(s - \delta_n, s + \delta_n)} \eta_n |u'_n|_+^2 dx + \int_{(s + \delta_n, b)} (\psi_n(v_n) |u'_n|_+^2 + |u'_n|_-^2) dx.$$

As $v_n \rightarrow 0$ we have $\psi_n(v_n) \rightarrow 1$ a.e. in (a, b) . By dominated convergence it follows that

$$\int_{(a, s - \delta_n)} (\psi_n(v_n) |u'_n|_+^2 + |u'_n|_-^2) dx \rightarrow \int_{(a, s)} (|u'|_+^2 + |u'|_-^2) dx = \int_{(a, s)} |u'|^2 dx.$$

The same reasoning can be applied to the interval $(s + \delta_n, b)$. Moreover,

$$\int_{(s - \delta_n, s + \delta_n)} \eta_n |u'_n|_+^2 dx = \eta_n (u(s + \delta_n) - u(s - \delta_n))^2 / 2\delta_n \rightarrow 0,$$

since $\eta_n = o(\delta_n)$ and $u(s + \delta_n) - u(s - \delta_n) \rightarrow \llbracket u(s) \rrbracket$. Thus (30) is proved.

Let us write

$$\int_{(a,b)} (\varepsilon_n^{-1} v_n^2 + \varepsilon_n |v'_n|^2 + \rho \varepsilon_n^3 |v''_n|^2) dx = \int_{(a, s - \delta_n)} (\varepsilon_n^{-1} v_n^2 + \varepsilon_n |v'_n|^2 + \rho \varepsilon_n^3 |v''_n|^2) dx + \int_{(s - \delta_n, s + \delta_n)} \varepsilon_n^{-1} dx + \int_{(s + \delta_n, b)} (\varepsilon_n^{-1} v_n^2 + \varepsilon_n |v'_n|^2 + \rho \varepsilon_n^3 |v''_n|^2) dx.$$

As $\delta_n = o(\varepsilon_n)$ we have

$$\int_{(s - \delta_n, s + \delta_n)} \varepsilon_n^{-1} dx = 2\delta_n \varepsilon_n^{-1} \rightarrow 0.$$

Moreover, by a simple change of variable,

$$\int_{(s + \delta_n, b)} (\varepsilon_n^{-1} v_n^2 + \varepsilon_n |v'_n|^2 + \rho \varepsilon_n^3 |v''_n|^2) dx = \int_0^{R_*} (w_* + |w'_*|^2 + \rho |w''_*|^2) dx = \mathcal{K}(w_*).$$

We can proceed in the same way in the interval $(a, s - \delta_n)$. The proof is concluded. \blacksquare

5 Numerical tests

In this section, we provide an extensive comparison between AT_1 , second- and fourth-order models. We can view the proposed fourth-order model (see §3) as an extension of the second-order phase-field functional, weighted by the coefficient ρ , which we initially set equal to 1 (a study of the dependence on ρ is given in §6). Consequently, we set $c_\rho = 4.4485$ and $R_* = 3.83$ and we analyze the numerical performance of our AT_1 fourth-order model, considering several benchmarks. First, a pure tensile test is carried out to assess the elastic limit and its relative error with respect to the theoretical expected value. In this case, we compare the results only for second- and fourth-order AT_1 functionals (since AT_2 does not define an elastic limit).

After that, three benchmarks well established in the phase-field literature for fracture are considered, namely the DCB ([5, 18]), the SEN tensile test [17, 18], and the SEN shear test [40]. To make the comparison more homogeneous, we set all the above examples with the same conditions, avoiding differences in geometry, material, and imposition of the initial pre-field. Therefore, in all these tests (see Figures 3b - 3d) the uncracked domain is a square with a side of 1 mm, a fracture toughness $G_c = 2.7 \cdot 10^{-3}$ kN/mm, an internal length $\varepsilon = 0.01$ mm, a Young's modulus $E = 210$ kN/mm², and a Poisson's ratio $\nu = 0.3$. In all these benchmarks, we compare second- and fourth-order AT_1 , based on a new definition of the mesh size in dependence of the R_* value (see §3.3), in terms of accuracy of the dissipated energy. More precisely, for each considered mesh, we compute the dissipated energy $\mathcal{D}_{\varepsilon,h}$ at the end of the analysis and the corresponding (sharp) crack length ℓ . Thus, the effective toughness G_c^{eff} is evaluated as:

$$G_c^{\text{eff}} = \frac{\mathcal{D}_{\varepsilon,h}}{\ell}. \quad (32)$$

Then, given the input toughness G_c , the relative error [5] is computed as:

$$\text{R.error} = \left| \frac{G_c^{\text{eff}} - G_c}{G_c} \right| = \left| \frac{\Delta G_c^{\text{eff}}}{G_c} \right|. \quad (33)$$

Note that, by Γ -convergence, $\mathcal{D}_{\varepsilon,h} \rightarrow G_c \ell$, therefore $G_c^{\text{eff}} \rightarrow G_c$ and $\text{R.error} \rightarrow 0$ (as $h \ll \varepsilon \ll 1$).

All the simulations are performed with quadratic C^1 -continuous B-Splines (for a comprehensive discussion on the definition of these isogeometric functions, readers may refer to [46, 25, 13] and references therein) to directly compare all the models as in [19] independently on the order of the functional.

5.1 Pure traction test

A pure traction test is considered to measure the difference in terms of the elastic limit value for the second- and fourth-order AT_1 models with respect to a reference analytical solution. In order to simulate a pure 1D traction test, a specimen with $t = 1$ mm and $b = 20$ mm is analyzed. Imposed horizontal displacements, mimicking a traction condition, are applied at $x = \pm b/2$ (see Figure 3a). For this benchmark, we consider a Young's modulus $E = 100$ kN/mm², a Poisson's ratio $\nu = 0$, an internal length $\varepsilon = 0.125$ mm, and a material toughness $G_c = 0.01$ kN/mm. Thus, the theoretical value σ_{th} of the elastic limit is computed as a function of the regularization parameter c_ρ , the material toughness G_c , and the shear modulus $\mu = E/(2(1 + \nu))$, and reads:

$$\sigma_{\text{th}} = \sqrt{\frac{2G_c\mu}{c_\rho\varepsilon}}. \quad (34)$$

The quasi-static displacement-controlled loading history consists of 2000 steps with uniform increments, starting from a minimum horizontal (boundary) displacement $u_{\text{min}} = 0$ mm up to a maximum horizontal displacement $u_{\text{max}} = 20 \cdot 10^{-2}$ mm.

All analyses are performed considering a uniform mesh with size $h = 0.0625$ mm and, in Figure 4, we report the crack patterns corresponding to the last loading steps for the second- and fourth-order AT_1 models¹.

¹Due to the homogenous response in terms of stress in the body for this test, a crack could nucleate anywhere in the

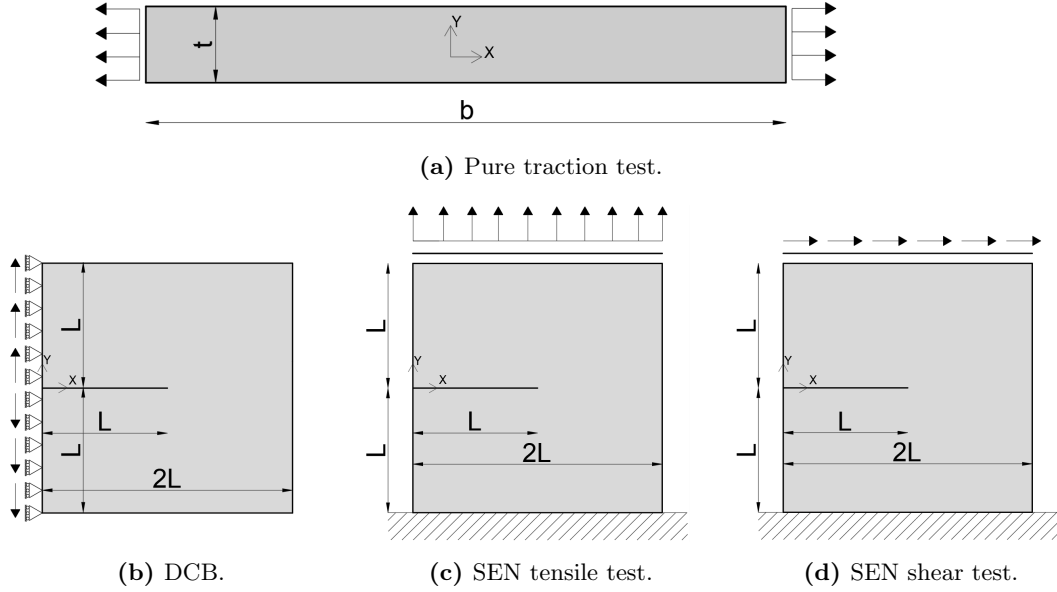


Figure 3: Geometry and boundary conditions for the considered numerical tests.

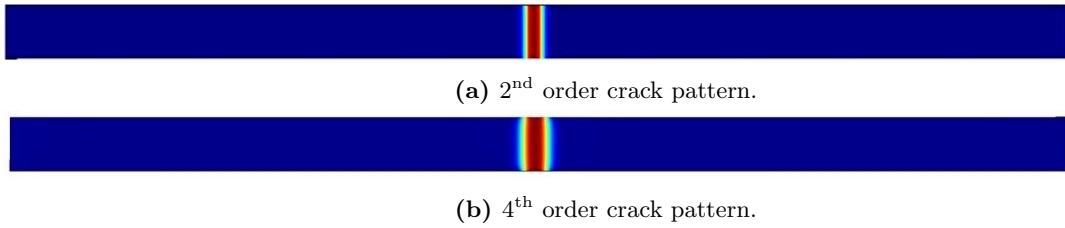


Figure 4: Last step crack patterns for the AT_1 models.

The elastic limits, obtained by computing the numerical stress at the step before crack onset (denoted by σ_c) are compared in Table 2 to σ_{th} (see Equation (34)), showcasing that the proposed AT_1 high-order model is able to correctly capture the stress peak, providing a relative error in line with the second-order AT_1 model.

Table 2: Pure traction test: relative percentage error.

AT_1 -model	σ_{th}	σ_c	R.error
[-]	[kN/mm ²]	[kN/mm ²]	[%]
2 nd order	1.73205	1.73200	0.00293
4 th order	1.34103	1.34101	0.00206

5.2 Mesh-size considerations and its appropriate selection

As far as the choice of the mesh size, we argue in the following way. From the theoretical point of view (see Theorem 2.5), the Γ -limit is recovered for $h \ll \varepsilon$, i.e., in the limit when the mesh size is much smaller

domain. Therefore, a small ($\sim 10^{-4}$) perturbation is applied at the center of the domain to allow the crack to nucleate in the middle of the specimen.

then the internal length. In practice, this condition means that the mesh size should be small enough to “resolve” the phase-field profile in its transition region, which is of order $R_*\varepsilon$. This observation entails an important consideration in the choice of the mesh size, crucial for the phase-field approach. From Proposition 3.1 and A.3, we know that $R_* \sim 3.8$ for the fourth order and $R_* = 2$ for the second order. Therefore, we choose

$$h = \frac{R_*\varepsilon}{n}, \text{ for } n = 4, 8, 16, \quad (35)$$

as reference mesh sizes for the both the AT_1 functionals. Note that, in this way, we provide also a set of results for roughly the same mesh (see for instance Figure 5) since $h = 0.005$ mm corresponds to $R_*\varepsilon/4$ for the second order and to $R_*\varepsilon/8$ for the fourth order. Actually, to better check the error trend of our fourth-order functional, we provide also the numerical results for $h = R_*\varepsilon/2$, clearly with $R_* = 3.83$. For AT_2 the above argument, based on R_* , does not apply, since the theoretical results would give $R_* = +\infty$, therefore, for a direct comparison we choose the mesh sizes corresponding to the second-order AT_1 .

Finally, in Figure 1 it can be seen how the 1D phase-field profile is influenced by progressively decreasing the coefficient ρ in front of the high-order term of the surface energy. As ρ decreases, the fourth-order optimal profile tends to the second-order optimal one, providing a “less” regular function with smaller crack width. As a consequence, in the parametric study of §6 we compare the numerical results obtained both by fixing the mesh size and linking it to ρ , through the value $R_*(\rho)$.

5.3 DCB test

The DCB test has been employed in [5, 18, 19] to compare low- and high-order AT_2 formulations. In our case, we consider a squared sample of side $2L = 1$ mm with an initial phase-field crack located at $y = 0$ mm and $x \in [0, L]$ mm, modeled by the interpolated phase-field variable (IPF) technique [19]. A quasi-static displacement-controlled loading history is applied at the left vertical edge (see Figure 3b) consisting of 37 loading steps, with a minimum vertical boundary displacement $u_{\min} = 0$ mm, a uniform increment $\Delta u = 5 \cdot 10^{-4}$ mm, and a maximum vertical boundary displacement $u_{\max} = 18 \cdot 10^{-3}$ mm, tuned to completely break the specimen. Additionally, we completely restrain the horizontal displacement at $x = 0$ mm.

We provide an extensive comparison of the proposed fourth-order AT_1 model with respect to the second-order one, as well as second- and fourth-order AT_2 models, such that for the second-order AT_1 the considered meshes are $h = R_*\varepsilon/4$, $h = R_*\varepsilon/8$. Instead, for the fourth-order AT_1 we consider $h = R_*\varepsilon/4$, $h = R_*\varepsilon/8$, and $h = R_*\varepsilon/16$, whereas for the classical second- and fourth-order AT_2 formulations we examine $h = \varepsilon/4$, $h = \varepsilon/8$. All AT_2 and the AT_1 second-order tests are performed with locally refined mesh, obtained using a non-uniform knot-vector, while all fourth-order AT_1 tests are performed with uniform meshes. Despite this difference in the mesh definition, the AT_1 fourth-order model showcases computational advantages even performing analyses with uniform mesh (see §7.1 for an in-depth discussion in terms of trade-off between accuracy and computational cost for all considered models on several benchmarks).

In Table 3, it can be observed that for the fourth-order AT_1 we have a smaller error values, allowing for a significant reduction in terms of degrees of freedom, and a higher convergence rate, in comparison with the other AT_1 model, computed as:

$$\text{CR} = \frac{\log((\Delta G_c^{\text{eff}})_{k+1}) - \log((\Delta G_c^{\text{eff}})_k)}{\log(h_{k+1}) - \log(h_k)}, \quad (36)$$

where k represent the loading steps, ΔG_c^{eff} is the toughness variation between two steps and h is the mesh size. This result also holds in the comparison with the AT_2 models as we can observe in Figure 5. Furthermore, we remark that, for this test, all AT_1 models are more accurate than the AT_2 ones and the proposed AT_1 fourth-order functional is able to provide more accurate results than all investigated classical literature models. More specifically, it can be seen observed for comparable meshes (namely in

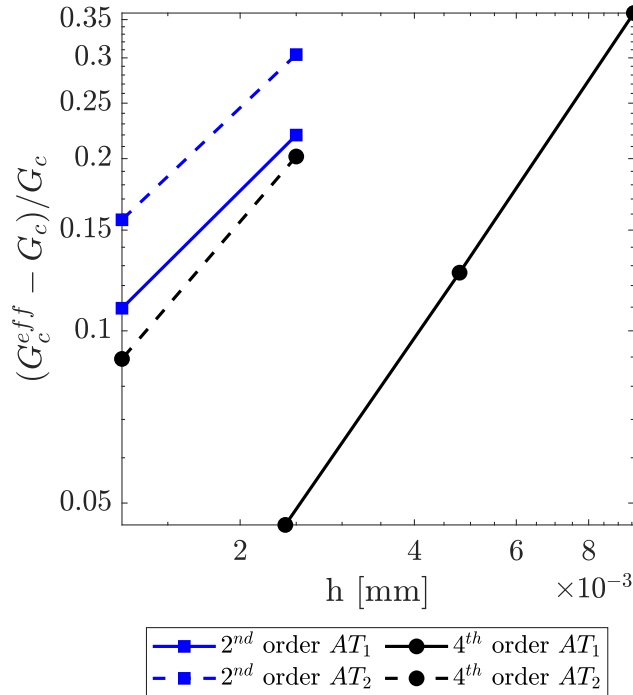


Figure 5: DCB test: accuracy analysis considering all AT -models represented in double logarithmic scale.

Table 3: DCB test: AT_1 model relative percent error on the toughness.

h [mm]	2 nd order [%]	4 th order [%]
$R_*\varepsilon/8$	21.99	12.63
$R_*\varepsilon/16$	10.95	4.50
CR [-]	1.01	1.51

the case of $h = R_*\varepsilon/16$) that the fourth-order AT_1 model shows a relative error on the toughness about ten times lower than the other models.

In Figure 6, we compare the phase-field contour plots for the AT_1 second-order and the novel AT_1 fourth-order formulations. It can be observed that the proposed model provides a thicker profile than the one obtained for the second-order formulation due to the higher regularity of the model. Nevertheless, the novel model allows for comparable values in terms of relative error on the toughness (see Table 3) showing a significant reduction of the relative error.

5.4 SEN tensile test

We consider now the SEN tensile test [40], another mode I fracture test leading to complete breakage of the specimen. Geometry and boundary conditions of this benchmark are summarized in Figure 3c. Also in this case, the initial pre-crack is located at $y = 0$ mm and $x \in [0, L] = [0, 0.5]$ mm and is modeled with the technique of the IPF. A quasi-static displacement-controlled loading history is applied at the

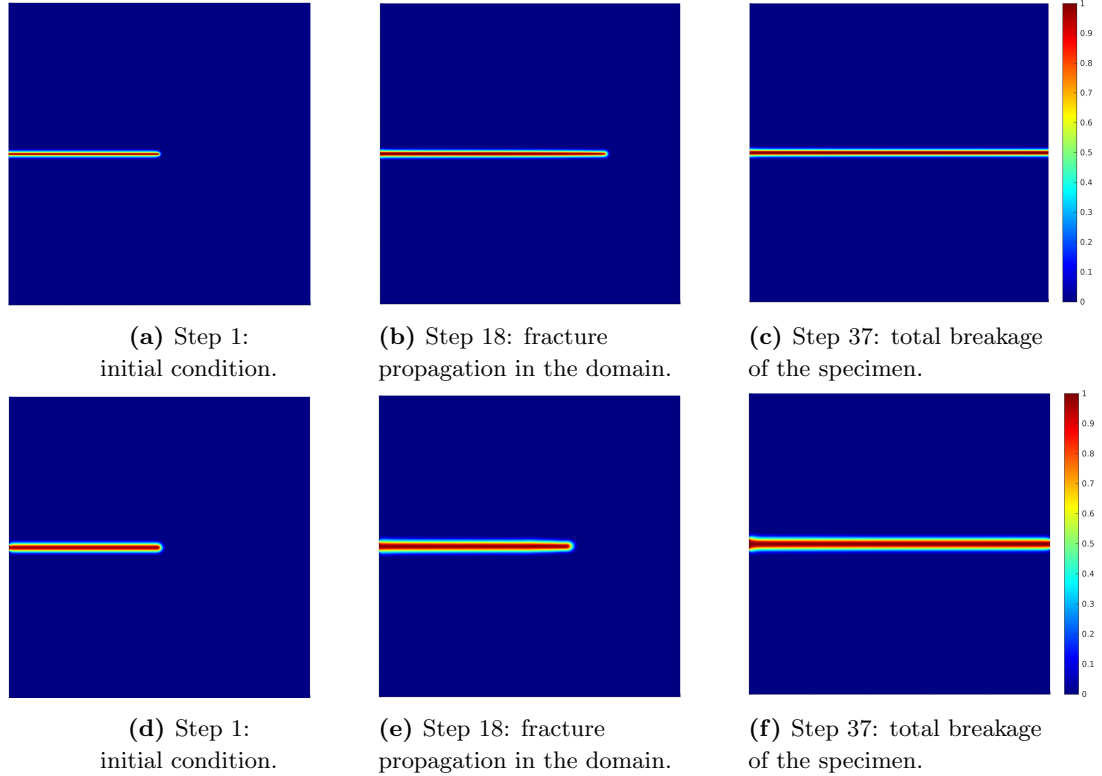


Figure 6: DCB test: crack patterns of three different loading steps for the AT_1 second-order (top row) and AT_1 fourth-order model (bottom row) considering $h = 0.0025$ mm.

top horizontal edge, comprising 21 loading steps, a minimum boundary displacement $u_{min} = 0$ mm, a uniform increment $\Delta u = 3 \cdot 10^{-4}$ mm, and a maximum boundary displacement $u_{max} = 6 \cdot 10^{-3}$ mm. Instead, we constrain the horizontal displacement at $y = L$. For this benchmark, we consider mesh sizes $h = R_*\varepsilon/4$ and $h = R_*\varepsilon/8$ for the AT_1 models, whereas for the AT_2 functionals we examine $h = \varepsilon/2$ and $h = \varepsilon/4$.

Let us comment on the accuracy trend reported in Figure 7: it can be observed that the proposed AT_1 model has a slope comparable with the AT_2 fourth-order model, however, for fixed mesh size, it is more accurate than the analyzed second-order models; resulting in practice in a significant reduction of the computational cost (see §7.1 for more details). Namely, it can be seen in Figure 7 that, for the fourth-order AT_1 model, if we refine the mesh from $h = R_*\varepsilon/4$ to $h = R_*\varepsilon/8$, the relative error on the toughness decreases from 7.41% to 1.73%. Also for this example, for comparable meshes, the AT_1 fourth-order model shows an error approximately ten times smaller than the error obtained with the other models and we observe that the AT_1 models are more accurate than the AT_2 functional counterparts. As expected, also for the SEN tensile test, it can be seen in Figure 8 that the proposed AT_1 model provides a smoother crack pattern than the AT_1 second-order model, but entails much lower values of relative error on the toughness for a fixed mesh size in all cases (see Table 4).

5.5 SEN shear test

To provide a more challenging crack pattern evolution, we consider the SEN shear test having material properties and geometry as in [17, 18, 19]. In our case, the SEN domain features an internal length $\varepsilon = 0.01$ mm and an initial pre-crack located at $y = 0$ and $x \in [0, L] = [0, 0.5]$ mm (see Figure 3d) modeled with the IPF technique. The specimen is loaded with a quasi-static displacement-controlled history consisting of 20 loading steps, with a minimum displacement $u_{min} = 6 \cdot 10^{-3}$ mm, a uniform increment $\Delta u = 3 \cdot 10^{-4}$ mm, and a maximum displacement $u_{max} = 12 \cdot 10^{-3}$ mm. Also in this case,

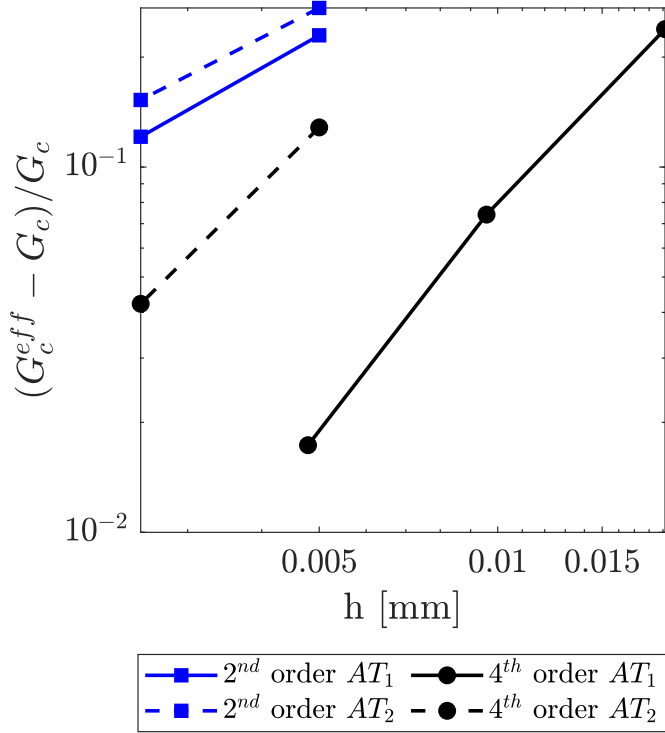


Figure 7: SEN tensile test: accuracy analysis considering all the AT -models.

Table 4: SEN tensile test: AT_1 model relative percent error on the toughness represented in double logarithmic scale.

h [mm]	2 nd order [%]	4 th order [%]
$R_*\varepsilon/4$	22.94	7.41
$R_*\varepsilon/8$	12.11	1.70
CR [-]	0.92	1.69

for the AT_1 models the considered mesh sizes comprise $h = R_*\varepsilon/4$ and $h = R_*\varepsilon/8$, whereas for the AT_2 formulations we examine $h = \varepsilon/2$ and $h = \varepsilon/4$.

We study the accuracy trend reported in Figure 9 and, again, we can observe that the novel AT_1 model showcases a higher slope when compared to the AT_2 fourth-order model and comparable accuracy with second-order models allowing for a significant reduction of the computational effort (about 90% of the degrees of freedom when using a mesh size $h = 0.0096$ mm). Additionally, we highlight that further refinement of the mesh preserves the convergence trend of the error, that decreases from 15.30% to 4.39%, confirming that also for this test in the case of comparable meshes the proposed AT_1 fourth-order model exhibits an error ten times lower than the ones provided by other models. In Figure 10, we compare the crack patterns obtained with both the proposed AT_1 fourth-order and AT_1 second-order model, remarking that our fourth-order AT_1 model provides a crack pattern which exhibits a kink due to the utilized coarse mesh. However, this tests confirms once again comparable values of relative error on

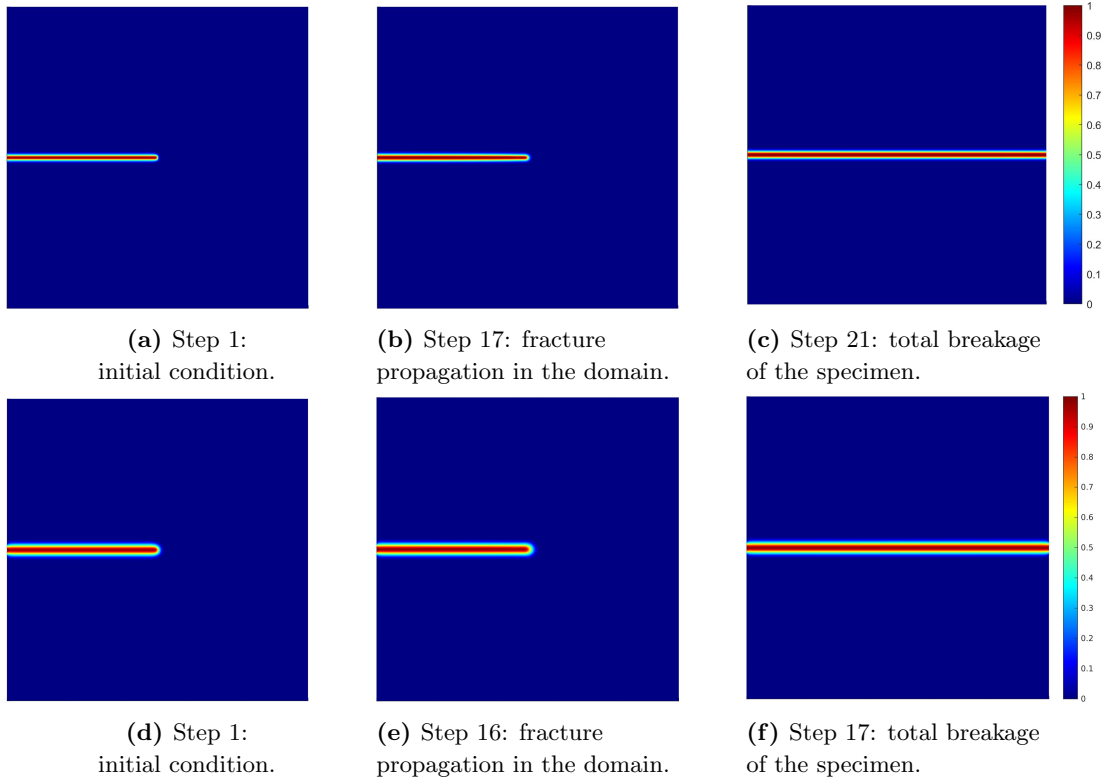


Figure 8: SEN tensile test: crack patterns of three different loading steps for the AT_1 second-order (top row) and AT_1 fourth-order model (bottom row) considering $h = 0.005$ mm.

the toughness (see Table 5) when comparing our AT_1 fourth-order formulation against the AT_1 low-order counterpart.

Table 5: SEN shear test: AT_1 model relative percent error on the toughness.

h	2 nd order	4 th order
[mm]	[%]	[%]
$R_*\varepsilon/4$	32.22	15.30
$R_*\varepsilon/8$	14.56	4.39
CR [-]	1.15	1.83

6 Parametric study on the coefficient ρ

In this section we study how the coefficient ρ , that weights the high-order term of the phase-field energy, affects the accuracy of the effective toughness as well as the elastic limit. To this end, we consider the following values: $\rho = 2^i$ for $i = -4, \dots, 4$.

6.1 Elastic limit comparison

Considering a variable coefficient associated to the laplacian term influences the value of the regularization parameter c_ρ from which depends the theoretical value of elastic limit. As in §5.1, we consider a pure traction test (see Figure 3a) for the proposed AT_1 model. The results are summarized in Table 6,

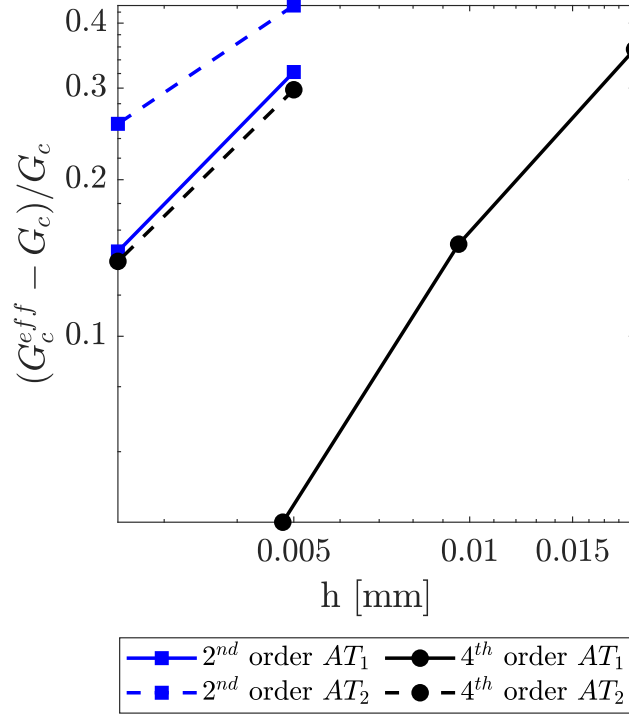


Figure 9: SEN shear test: accuracy analysis considering all the AT -models represented in double logarithmic scale.

highlighting a minimum value in terms of relative error for $\rho = 1$, that appears to be a good choice to perform all analyses. Furthermore, it can be observed that the value of R_* is increasing with respect to ρ and, consequently, the mesh size $h \sim R_*\varepsilon$ is increasing with respect to ρ . Thus, other possible choices of ρ balance the trade off between accuracy and computation time.

Table 6: Pure traction test: relative percentage error on the elastic limit for a fixed mesh corresponding to the reference case $\rho = 1$ (i.e., $R_* = 3.83$).

ρ	R_*	c_ρ	σ_{th}	σ_c	R.err
[-]	[-]	[-]	[kN/mm ²]	[kN/mm ²]	[%]
16	7.1041	7.7811	1.0140	1.0199	0.5871
8	6.0364	6.6769	1.0946	1.0973	0.2440
4	5.1514	5.7717	1.1773	1.1784	0.0929
2	4.4230	5.0369	1.2603	1.2605	0.0197
1	3.8300	4.4485	1.3410	1.3410	0.0026
1/2	3.3554	3.9852	1.4168	1.4167	0.0115
1/4	2.9847	3.6281	1.4849	1.4848	0.0101
1/8	2.7045	3.3593	1.5432	1.5430	0.0123
1/16	2.4998	3.1615	1.5907	1.5900	0.0468

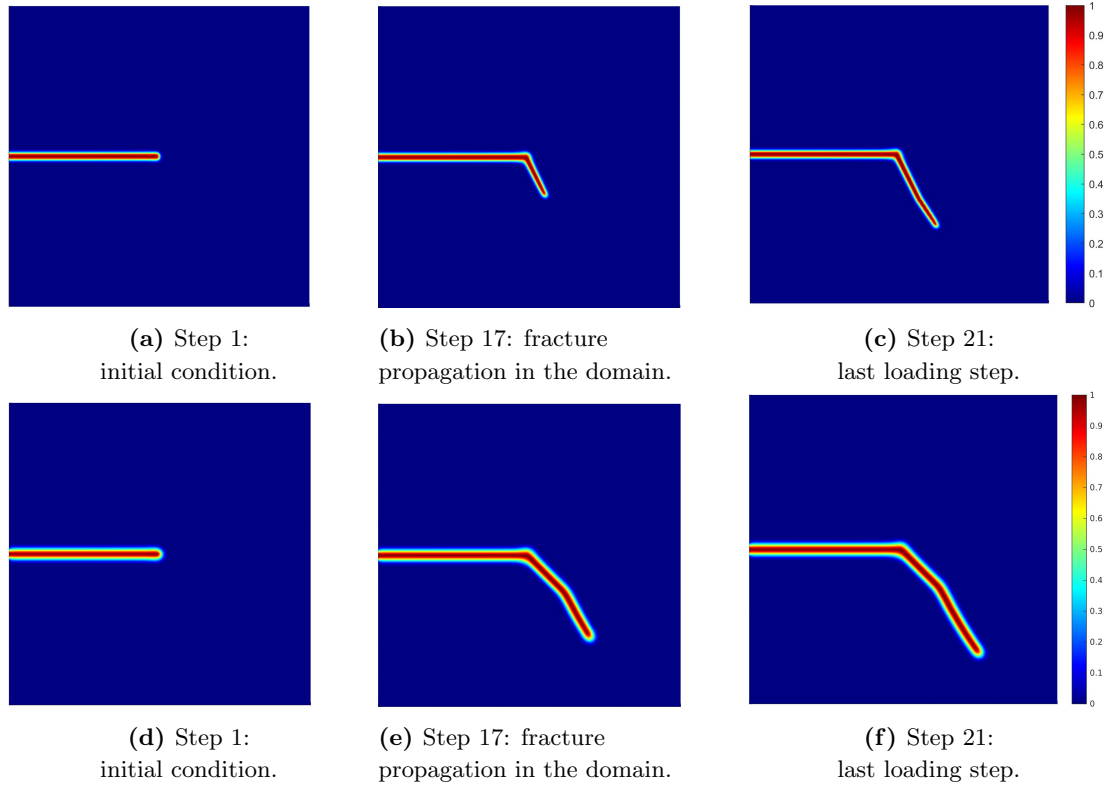


Figure 10: SEN shear test: crack patterns of three different loading steps for the AT_1 second-order (top row) and AT_1 fourth-order model (bottom row) considering $h = 0.005$ mm.

6.2 Toughness accuracy

To evaluate the toughness accuracy as a function of ρ , the SEN tensile and the SEN shear tests are reconsidered, providing respectively a mode I and mode II fracture benchmark. All analyses feature mesh size $h(R_*) = R_*\varepsilon/4$, where $R_* = 3.83$, namely the value in the reference case $\rho = 1$. In Figure

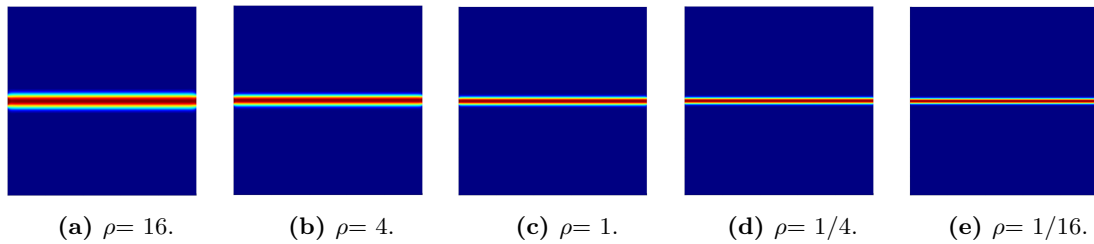


Figure 11: SEN tensile test: influence of the variation of the ρ coefficient on the final crack pattern for a fixed mesh size.

11, it can be observed that for the SEN traction test as the ρ coefficient decreases, the fracture width is reduced. The same behavior can be noticed also for the SEN shear benchmark in Figure 12. Additionally, we notice in this latter case that the crack length corresponding to the last loading step reduces as ρ decreases.

In Figure 13a, we highlight that for the SEN tensile test the relative error on the toughness is reducing while the ρ laplacian coefficient increases. This is due to the fact that by increasing the coefficient related to the higher-order term, the values of R_* increase and, consequently, the profile exhibits a wider shape. This observation underlines the influence of the parameter R_* on the mesh size that will be the object of an in-depth study in the next section. Also in the case of the SEN shear test (see Figure 13b) the relative

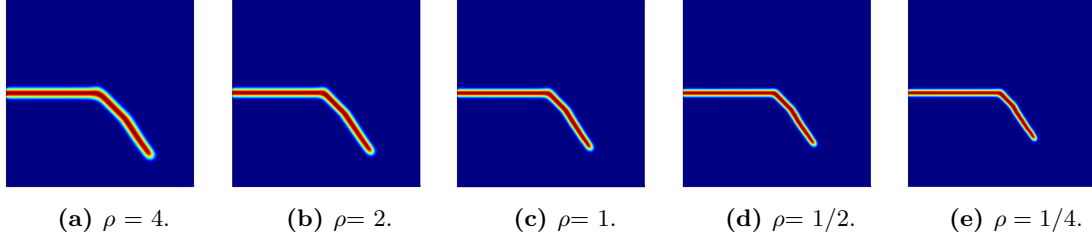


Figure 12: SEN shear test: influence of the variation of the ρ coefficient on the final crack pattern for a fixed mesh size.

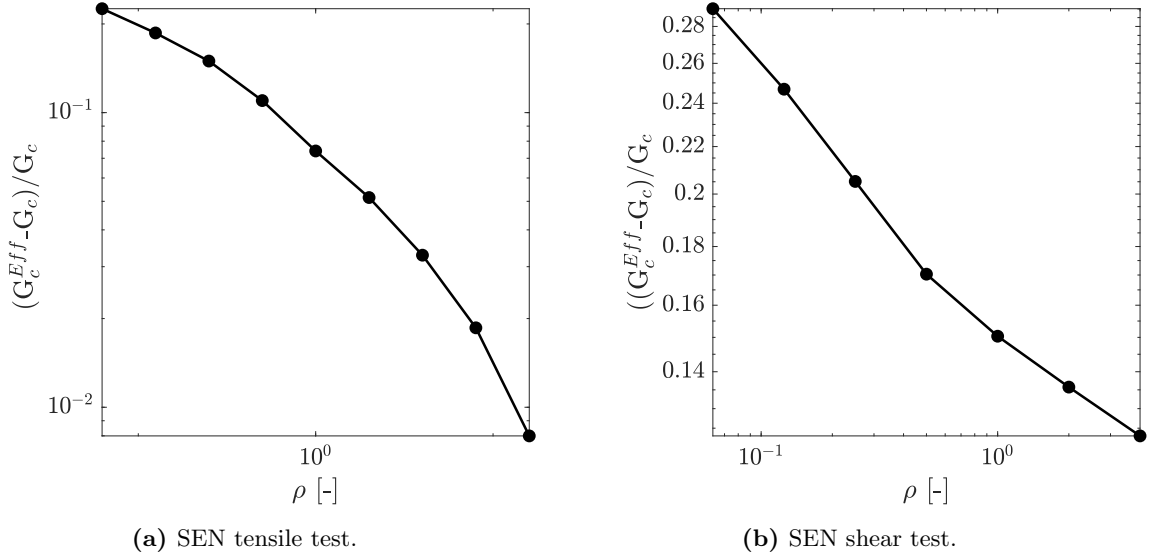


Figure 13: Trend of the relative error on the toughness for the SEN traction (left) and SEN shear (right) tests as a function of the ρ coefficient for a fixed mesh level.

error on the toughness decreases as the coefficient ρ increases. However, for this latter test a significantly high value of the ρ coefficient provides an inaccurate crack pater that is far from the reference one in the literature. Therefore, we omit this result in Figure 13b and prefer to represent the error trend only in the interval $\rho \in [1/16 - 4]$.

7 Trade-off between accuracy and computational cost

As the proposed AT_1 high-order model allows to perform simulation with higher accuracy, we focus in this section on assessing the computational cost in terms of necessary number of control points for a fixed and comparable level of accuracy with respect to the identified reference models in the literature. More specifically, in §7.1 we set an acceptable range of error and study how much the mesh can be coarsened, whereas in §7.2 we study the R_* value influence on the mesh size and the accuracy.

7.1 AT_1 - AT_2 comparisons for different mesh sizes

While performing numerical simulations, it is of primal importance to balance the trade-off between providing reliable results and keeping the computational effort of the analyses to an acceptable level. Thus, we herein focus again on two of the benchmarks discussed in §5, namely the SEN shear and traction tests, and we assess the computational gain in terms of number of utilized control points for

a fixed level of error on the fracture toughness. First, we focus on the SEN shear benchmark, which is modeled using a uniform quadratic C^1 IgA mesh and we observe in Table 7 that, for a fixed toughness error of about 15%, the AT_1 high-order model needs 11,664 control points, whereas all other AT -models² utilize 161,604 degrees of freedom. Consequently, we have in this case a saving in terms of control points of $\sim 93\%$. Then, we analyze the SEN tensile test, which considers a non-uniform knot vector in the case of all AT_2 and the AT_1 low-order models, whereas, even considering a uniform mesh for the AT_1 fourth order model, we obtain a saving of $\sim 43\%$ in terms of control points (see Table 8) to reach an error level of $\sim 10\%$.

Table 7: SEN shear test: number of control points for a fixed value of error on the toughness.

Error	2 nd order		4 th order	
	AT_1	AT_2	AT_1	AT_2
~ 15	161,604	-	11,664	161,604

Table 8: SEN tensile test: number of control points for a fixed value of error on the toughness.

Error	2 nd order		4 th order	
	AT_1	AT_2	AT_1	AT_2
~ 10	20,100	20,100	11,664	20,100

7.2 Influence of the R_* parameter

In §6, we investigate how the different values of R_* change the elastic limit (see Table 6) as well as the crack pattern width. All these considerations are made for a fixed mesh size (referring to the mesh size of the case considering $\rho = 1$, $R_* = 3.83$). However, the mesh-size definition in Equation (35) allows to considerably reduce the number of elements of a simulations for higher values of the ρ coefficient. Namely, the user has the choice to balance the trade-off between having a very accurate simulation (considering a mesh size equal to the one utilized for the AT_2 -model analyses) or less accurate results (providing an acceptable level of error) but faster simulations by taking into account the R_* parameter in the mesh size definition. To investigate this latter possibility, we performed the SEN tensile and SEN shear tests changing the mesh size as in Equation (35) for our fourth-order formulation and we observed that, for the SEN tensile test (see Figure 14), there is not a significant variation in the crack pattern. However, in the SEN shear test case (see Figure 15), choosing a mesh size based on the R_* value as in Equation (35) leads to a comparable fracture length with a smoother crack pattern. It can be observed also that reducing the coefficient ρ the curvature of the fracture makes a difference, reaching the one obtained for the second-order models and the fourth-order AT_2 , where the coefficient $\rho = 1/16$.

In Figure 16, we compare, for varying ρ , the relative percentage error on the toughness for a fixed mesh, corresponding to the reference case $\rho = 1$ (i.e., $R_* = 3.83$), and for a mesh varying with R_* (i.e., $h(R_*)$), namely a mesh size computed using Equation (35) with $n = 4$. It can be observed that, for both the SEN tensile and shear tests, the error range for the $h(R_*)$ case is smaller than the one obtained for a fixed mesh, as this latter choice overestimates the required mesh-size value, being approximately twice larger than the one needed to accurately resolve the internal length, leading to a higher error in the toughness. Conversely, for ρ grater than 1 the mesh size is underestimated, thereby entailing a lower

²We remark that the AT_2 second-order model has been excluded from this discussion because it is out of scale. In fact, as Figure 9 clearly highlights, it would need even more control points than the considered AT_1 second-order and AT_2 fourth-order models.

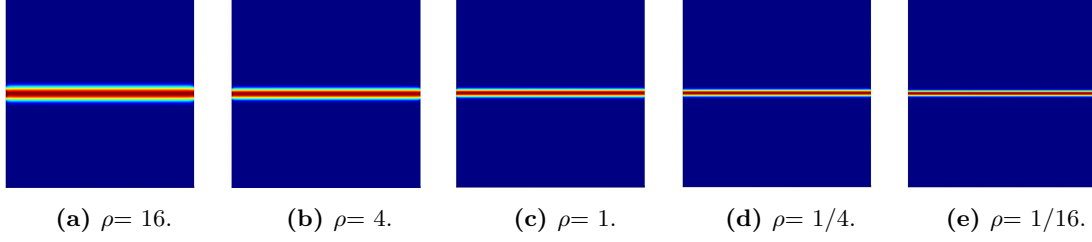


Figure 14: SEN tensile test: influence of the variation of coefficient ρ on the final crack pattern for mesh size computed as a function of the R_* parameter.

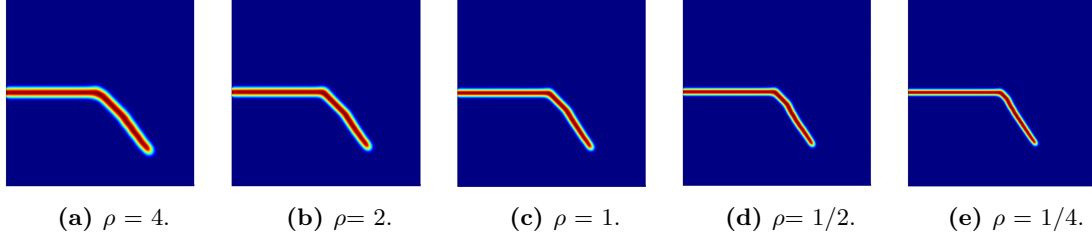
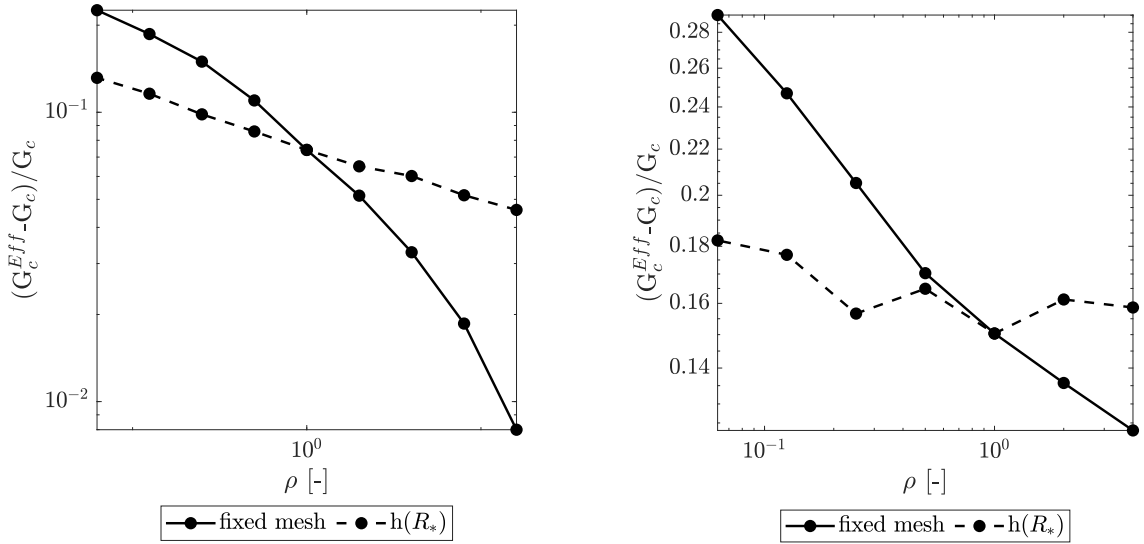


Figure 15: SEN shear test: influence of the variation of coefficient ρ on the final crack pattern for mesh size computed as a function of the R_* parameter.



(a) SEN tensile test.

(b) SEN shear test.

Figure 16: Influence of the mesh size on the relative error on the toughness for the SEN tensile and shear tests: comparison for fixed a mesh, corresponding to the reference case $\rho = 1$ (i.e., $R_* = 3.83$), and for a mesh varying with R_* .

accuracy. Then, we focus on the influence of the mesh on the elastic limit in the pure traction case and we highlight in Table 9 that the numerical values of the elastic limit computed either for a fixed mesh corresponding to the ρ reference case, σ_c , or for a mesh varying with R_* , $\sigma_c(R_*)$, are comparable, so as, consequently, their corresponding relative errors on the elastic limit. This entails a possible significant reduction in terms of the total number of required control points to reach satisfactory results for this test.

Table 9: Pure traction test: comparison between relative percent errors (i) for a fixed mesh size R_{err} (i.e., corresponding to the reference case $\rho = 1$) and (ii) for meshes varying with R_* ($R_{\text{err}}(R_*)$).

ρ	R_*	c_ρ	σ_{th}	σ_c	$\sigma_c(R_*)$	R.err	R.err(R_*)
[-]	[-]	[-]	[kN/mm ²]	[kN/mm ²]	[kN/mm ²]	[%]	[%]
16	7.1041	7.7811	1.0140	1.0199	1.0198	0.5871	0.5776
8	6.0364	6.6769	1.0946	1.0973	1.0973	0.2440	0.2431
4	5.1514	5.7717	1.1773	1.1784	1.1784	0.0929	0.0936
2	4.4230	5.0369	1.2603	1.2605	1.2605	0.0197	0.0198
1	3.8300	4.4485	1.3410	1.3410	1.3410	0.0026	0.0026
1/2	3.3554	3.9852	1.4168	1.4167	1.4167	0.0115	0.0116
1/4	2.9847	3.6281	1.4849	1.4848	1.4848	0.0101	0.0102
1/8	2.7045	3.3593	1.5432	1.5430	1.5430	0.0123	0.0123
1/16	2.4998	3.1615	1.5907	1.5900	1.5900	0.0468	0.0468

8 Conclusions

In this work, an AT_1 fourth-order model for phase-field brittle fracture is proposed. First, we prove a Γ -convergence result with a fine study of the optimal profile, providing (a) the explicit value of the corrector factor for the surface energy and (b) the explicit value of the width of the transition region.

Numerically, we employ an IgA framework that allows to discretize the high-order differential operator thanks to the smoothness of the isogeometric shape functions, highlighting once again the straightforward capability of IgA to model high-order PDEs. We study the performance of our fourth-order functional in terms of accuracy, as far as the elastic limit and the effective toughness.

About the accuracy in the evaluation of the toughness, we observed that the proposed AT_1 fourth-order model is more accurate than the classical AT ones present in the literature. These results confirm our findings in [19], pointing out that (in terms of accuracy) our fourth-order AT_1 formulation attains the same level of accuracy as other AT -formulations at a lower cost.

We also propose defining the mesh size as a function of the width of the phase-field profile, as characterized by Γ -convergence, leading to a significant reduction in the number of degrees of freedom.

Finally, a parametric analysis on the weight of the higher-order term seems to indicate that, even though there is not a specific set of coefficients providing significantly better results, high values of ρ give more regularity to the solution, tend to reduce errors, and allow for larger mesh sizes. Among future works, we will extend current formulation to simulate fracture in other structural elements such as Kirchhoff-Love shells and study its performance in dynamics. Furthermore, we will possibly include in the present simulation framework adaptive THB-spline refinement and multi-patch geometries [8].

Acknowledgements

L. Greco gratefully acknowledges the “Erasmus + Traineeship 2023/24” and “Bando di mobilità internazionale - 15a edizione” programmes, that partially supported him within the collaboration between the University of Pavia and the Universität der Bundeswehr München.

A. Reali is a member of the Gruppo Nazionale Calcolo Scientifico-Istituto Nazionale di Alta Matematica (GNCS-INDAM), and acknowledges the support of the Italian Ministry of University and Research (MUR) through the PRIN project COSMIC (No. 2022A79M75), funded by the European Union - Next Generation EU, as well as the contribution of the National Recovery and Resilience Plan, Mission

E. Maggiorèlli and M. Negri are members of the Gruppo Nazionale Analisi Matematica Probabilità Applicazioni-Istituto Nazionale di Alta Matematica (GNAMPA-INDAM) and acknowledge the support of the Italian Ministry of University and Research (MUR) through the PRIN project “Variational methods for stationary and evolution problems with singularities and interfaces” (No. 2022J4FYNJ).

A Optimal profile for the second-order AT_1 model

In this section, we provide a study of the optimal profile for the second-order AT_1 functional. Although the results are well known, here we provide a new proof along the lines of §3.

Let $\mathcal{U} = H^1(a, b)$ be the space of the admissible displacements and let $\mathcal{V} = H^1((a, b); [0, 1])$ be the set of the admissible phase-field functions. For $\varepsilon > 0$ and $\eta_\varepsilon = o(\varepsilon)$, let $\mathcal{F}_\varepsilon : L^1(a, b) \times L^1(a, b) \rightarrow [0, +\infty]$ be the AT_1 (second-order) functional defined by

$$\mathcal{F}_\varepsilon(u, v) = \begin{cases} \int_{(a,b)} (\kappa\psi_\varepsilon(v)|u'_+|^2 + \kappa|u'_-|^2) dx + \frac{G_c}{c} \int_{(a,b)} (\varepsilon^{-1}v + \varepsilon|v'|^2) dx & (u, v) \in \mathcal{U} \times \mathcal{V}, \\ +\infty & \text{otherwise,} \end{cases} \quad (37)$$

where $\psi_\varepsilon(v) = (v - 1)^2 + \eta_\varepsilon$ while $c > 0$ will be given later. Let $\mathcal{F} : L^1(a, b) \times L^1(a, b) \rightarrow [0, +\infty]$ be the functional

$$\mathcal{F}(u, v) = \begin{cases} \int_{(a,b) \setminus J_u} \kappa|u'|^2 dx + G_c \# J_u & \text{if } u \in SBV^2(a, b) \text{ with } \llbracket u \rrbracket > 0 \text{ and } v = 0 \text{ a.e. in } (a, b), \\ +\infty & \text{otherwise.} \end{cases} \quad (38)$$

In [9], the value c is provided explicitly and is given by

$$c = 4 \int_0^1 v^{1/2} = 8/3.$$

Here, we provide a different proof employing the explicit computation of the optimal profile following the lines of §3. To this end, let $\mathcal{K} : \mathcal{W} \rightarrow \mathbb{R}$ be defined by

$$\mathcal{K}(w) = \int_{(0, +\infty)} (w + |w'|^2) ds$$

where $\mathcal{W} = \{w \in L^1(\mathbb{R}_+) : w' \in L^2(\mathbb{R}_+), w(0) = 1\}$ is the domain of \mathcal{K} .

Proposition A.1. *There exists a unique*

$$w_* \in \operatorname{argmin} \{\mathcal{K}(w) : w \in \mathcal{W} \text{ such that } 0 \leq w \leq 1\}.$$

Moreover, $\operatorname{supp}(w_) = [0, R_*]$, where $R_* > 0$ is characterized in Proposition 3.1.*

Proof. Take $\{w_n\}_{n \in \mathbb{N}}$ such that $\mathcal{K}(w_n) \rightarrow \inf\{\mathcal{K}(w) : w \in \mathcal{W} \text{ such that } 0 \leq w \leq 1\}$. Observe that the functions w_n are bounded in $H^1(\mathbb{R}_+)$. Indeed, being $0 \leq w_n \leq 1$, we have $\|w_n\|_{H^1(\mathbb{R}_+)}^2 = \int_{\mathbb{R}_+} (|w_n|^2 + |w'_n|^2) dx \leq \int_{\mathbb{R}_+} (|w_n| + |w'_n|^2) dx < +\infty$. Therefore, it exists a (non-relabelled) subsequence of $\{w_n\}_{n \in \mathbb{N}}$ that weakly converges in $H^1(\mathbb{R}_+)$ to a certain $w_* \in H^1(\mathbb{R}_+)$. The set $\{w \in \mathcal{W} : 0 \leq w \leq 1\}$ is weakly closed (being convex and strongly closed) in $H^1(\mathbb{R}_+)$ and hence w_* belongs to this set. Now, since the functional \mathcal{K} is weakly lower semicontinuous (being strictly convex), we obtain that w_* is indeed the unique minimum in definition (4). \blacksquare

Theorem A.2. *Let $c = 2\mathcal{K}(w_*)$. Then \mathcal{F}_ε Γ -converge to \mathcal{F} as $\varepsilon \rightarrow 0^+$ with respect to the (strong) topology of $L^1(a, b) \times L^1(a, b)$.*

In order to characterize w_* , R_* , and c , it is convenient to introduce for $R \in (0, +\infty)$ the localized energies $\mathcal{K}_R : \mathcal{W}_R \rightarrow \mathbb{R}$ given by

$$\mathcal{K}_R(w) = \int_{(0, R)} (w + |w'|^2) dx,$$

where $\mathcal{W}_R = \{w \in H^1(0, R) : w(0) = 1, w(R) = 0\}$. We will also employ the local unconstrained optimal profiles

$$w_R \in \operatorname{argmin} \{\mathcal{K}_R(w) : w \in \mathcal{W}_R\}.$$

Clearly, the above minimizer is unique and it is characterized by the ODE

$$\begin{cases} 1 - 2w'' = 0 & \text{on } (0, R) \\ w(0) = 1 \\ w(R) = 0. \end{cases}$$

Hence $w_R(x) = \frac{1}{4}x^2 - \frac{1}{R}(1 + \frac{1}{4}R^2)x + 1$. In analogy with §3, the relationship between the local unconstrained profiles w_R and the optimal profile w_* is given by the following Proposition.

Proposition A.3. *It holds $R_* = \max\{R \in (0, +\infty) : w_R \in [0, 1]\} = 2$, moreover, $w_*|_{[0, R_*]}(x) = w_{R_*}(x)$, i.e., $w_*(x) = \frac{1}{4}x^2 - x + 1$.*

Proof. Since w_R is quadratic and convex, with $w_R(0) = 1$ and $w_R(R) = 0$, requiring that $w_R \in [0, 1]$ is equivalent to asking that $w'_R(R) \leq 0$, that gives that $R \leq 2$, hence $\max\{R \in (0, +\infty) : w_R \in [0, 1]\} = 2$.

Notice that $w_*(x) < 1$ for all $x > 0$. Indeed, if it existed $R' > 0$ such that $w_*|_{[0, R']} = 1$, then $\hat{w}(x) = w_*(x + R')$ would be such that $\mathcal{K}(\hat{w}) < \mathcal{K}(w_*)$, that is absurd. We define $R_* := \inf\{x : w_*(x) = 0\}$ and obviously $w_*|_{[R_*, +\infty)} = 0$. Now, $w_*|_{[0, R_*]}$ is the minimizer of \mathcal{K}_{R_*} with boundary conditions $w(0) = 1$ and $w(R_*) = 0$ and with the constraint $w_* \in [0, 1]$. However, $0 < w_*(x) < 1$ for $x \in (0, R_*)$ (by definition of R_*), hence $d\mathcal{K}(w_*)[\xi] = 0$ for every $\xi \in C_c^\infty(0, R_*)$, which means that w_* solves the Euler-Lagrange equation

$$\begin{cases} 1 - 2w_*'' = 0 & \text{on } (0, R_*) \\ w_*(0) = 1 \\ w_{R_*}(R_*) = 0. \end{cases} \quad (39)$$

In other terms, $w_*|_{[0, R_*]}(x) = w_{R_*}(x)$. As a straightforward consequence, since $w_* \in [0, 1]$, $R_* \leq \max\{R \in (0, +\infty) : w_R \in [0, 1]\} = 2$.

On the other hand, $w_2 \in \operatorname{argmin} \{\mathcal{K}_2(w) : w \in \mathcal{W}_2\}$. Since $w_2 \in [0, 1]$ we also have $w_2 \in \operatorname{argmin} \{\mathcal{K}_2(w) : w \in \mathcal{W}_2, w \in [0, 1]\}$. Observe that $w_*|_{[0, 2]} \in \operatorname{argmin} \{\mathcal{K}_2(w) : w \in \mathcal{W}_2, w \in [0, 1]\}$ (indeed $R_* < 2$ and $w_*|_{[R_*, +\infty)} = 0$) and by the uniqueness of the minimizer $w_*|_{[0, 2]} = w_2 = \frac{1}{4}(x - 2)^2$. Hence $R_* = 2$. ■

Proposition A.4. *The explicit value of the optimal constant is $c = \frac{8}{3}$.*

Proof. The constant c is given by $2\mathcal{K}(w_*)$. By direct calculations we get that $c = R_* - \frac{1}{24}R_*^3 + \frac{2}{R_*}$ and since $R_* = 2$, then $c = \frac{8}{3}$. ■

References

- [1] M. Ambati and L. De Lorenzis. Phase-field modeling of brittle and ductile fracture in shells with isogeometric NURBS-based solid-shell elements. *Computer Methods in Applied Mechanics and Engineering*, 312:351–373, 2016.

- [2] M. Ambati, T. Gerasimov, and L. De Lorenzis. A review on phase-field models of brittle fracture and a new fast hybrid formulation. *Computational Mechanics*, 55:383–405, 2015.
- [3] L. Ambrosio and V.M. Tortorelli. Approximation of functionals depending on jumps by elliptic functionals via Γ -convergence. *Comm. Pure Appl. Math.*, 43(8):999–1036, 1990.
- [4] H. Amor, J.-J. Marigo, and C. Maurini. Regularized formulation of the variational brittle fracture with unilateral contact: Numerical experiments. *Journal of the Mechanics and Physics of Solids*, 57(8):1209–1229, 2009.
- [5] M.J. Borden, T.J.R. Hughes, C.M. Landis, and C.V. Verhoosel. A higher-order phase-field model for brittle fracture: Formulation and analysis within the isogeometric analysis framework. *Computer Methods in Applied Mechanics and Engineering*, 273:100–118, 2014.
- [6] B. Bourdin, G.A. Francfort, and J.-J. Marigo. Numerical experiments in revisited brittle fracture. *Journal of the Mechanics and Physics of Solids*, 48(4):797–826, 2000.
- [7] B. Bourdin, G.A. Francfort, and J.-J. Marigo. The variational approach to fracture. *J. Elasticity*, 91:5–148, 2008.
- [8] C. Bracco, C. Giannelli, A. Reali, M. Torre, and R. Vázquez. Adaptive isogeometric phase-field modeling of the cahn–hilliard equation: Suitably graded hierarchical refinement and coarsening on multi-patch geometries. *Computer Methods in Applied Mechanics and Engineering*, 417:116355, 2023.
- [9] A. Braides. *Approximation of Free-Discontinuity Problems*. Springer-Verlag, Berlin, 1998.
- [10] J. Bueno and H. Gómez. Liquid-vapor transformations with surfactants. Phase-field model and Isogeometric Analysis. *Journal of Computational Physics*, 321:797–818, 2016.
- [11] M. Burger, T. Esposito, and C.I. Zeppieri. Second-order edge-penalization in the Ambrosio-Tortorelli functional. *Multiscale Model. Simul.*, 13(4):1354–1389, 2015.
- [12] A. Chambolle, S. Conti, and G.A. Francfort. Approximation of a brittle fracture energy with a constraint of non-interpenetration. *Arch. Ration. Mech. Anal.*, 228(3):867–889, 2018.
- [13] J.A. Cottrell, T.J.R. Hughes, and A. Reali. Studies of refinement and continuity in isogeometric structural analysis. *Computer Methods in Applied Mechanics and Engineering*, 196(41):4160–4183, 2007.
- [14] G. Dal Maso. *An introduction to Γ -convergence*. Birkhäuser, Boston, 1993.
- [15] R.P. Dhote, H. Gomez, R.N.V. Melnik, and J. Zu. 3D coupled thermo-mechanical phase-field modeling of shape memory alloy dynamics via isogeometric analysis. *Computers & Structures*, 154:48–58, 2015.
- [16] P. Farrell and C. Maurini. Linear and nonlinear solvers for variational phase-field models of brittle fracture. *International Journal for Numerical Methods in Engineering*, 109(5):648–667, 2017.
- [17] T. Gerasimov and L. De Lorenzis. On penalization in variational phase-field models of brittle fracture. *Computer Methods in Applied Mechanics and Engineering*, 354:990–1026, 2019.
- [18] S. Goswami, C. Anitescu, and T. Rabczuk. Adaptive fourth-order phase field analysis for brittle fracture. *Computer Methods in Applied Mechanics and Engineering*, 361:112808, 2020.
- [19] L. Greco, A. Patton, M. Negri, A. Marengo, U. Perego, and A. Reali. Higher order phase-field modeling of brittle fracture via isogeometric analysis. *Engineering with Computers*, 2024.

- [20] A.A. Griffith. The phenomena of rupture and flow in solids. *Phil. Trans. Roy. Soc. London*, 18:163–198, 1920.
- [21] H. Gómez, V.M. Calo, Y. Bazilevs, and T.J.R. Hughes. Isogeometric analysis of the Cahn–Hilliard phase-field model. *Computer Methods in Applied Mechanics and Engineering*, 197(49):4333–4352, 2008.
- [22] H. Gómez, T.J.R. Hughes, X. Nogueira, and V.M. Calo. Isogeometric analysis of the isothermal Navier–Stokes–Korteweg equations. *Computer Methods in Applied Mechanics and Engineering*, 199(25):1828–1840, 2010.
- [23] T. Heister, M.F. Wheeler, and T. Wick. A primal-dual active set method and predictor-corrector mesh adaptivity for computing fracture propagation using a phase-field approach. *Computer Methods in Applied Mechanics and Engineering*, 290:466–495, 2015.
- [24] C. Hesch, S. Schuß, M. Dittmann, M. Franke, and K. Weinberg. Isogeometric analysis and hierarchical refinement for higher-order phase-field models. *Comput. Methods Appl. Mech. Engrg.*, 303:185–207, 2016.
- [25] T.J.R. Hughes, J.A. Cottrell, and Y. Bazilevs. Isogeometric analysis: CAD, finite elements, NURBS, exact geometry and mesh refinement. *Computer Methods in Applied Mechanics and Engineering*, 194(39):4135–4195, 2005.
- [26] R. Kiran, N. Nguyen-Thanh, H. Yu, and K. Zhou. Adaptive isogeometric analysis–based phase-field modeling of interfacial fracture in piezoelectric composites. *Engineering Fracture Mechanics*, 288:109181, 2023.
- [27] R. Kiran, N. Nguyen-Thanh, and K. Zhou. Adaptive isogeometric analysis–based phase-field modeling of brittle electromechanical fracture in piezoceramics. *Engineering Fracture Mechanics*, 274:108738, 2022.
- [28] D. Knees and M. Negri. Convergence of alternate minimization schemes for phase field fracture and damage. *Math. Models Methods Appl. Sci.*, 27(9):1743–1794, 2017.
- [29] D. Knees, R. Rossi, and C. Zanini. A vanishing viscosity approach to a rate-independent damage model. *Math. Models Methods Appl. Sci.*, 23(4):565–616, 2013.
- [30] P. Li, W. Li, B. Li, S. Yang, Y. Shen, Q. Wang, and K. Zhou. A review on phase field models for fracture and fatigue. *Engineering Fracture Mechanics*, 289:109419, 2023.
- [31] Y. Li, T. Yu, and S. Natarajan. An adaptive isogeometric phase-field method for brittle fracture in rock-like materials. *Engineering Fracture Mechanics*, 263:108298, 2022.
- [32] Y. Li, T. Yu, S. Natarajan, and T.Q. Bui. A dynamic description of material brittle failure using a hybrid phase-field model enhanced by adaptive isogeometric analysis. *European Journal of Mechanics - A/Solids*, 97:104783, 2023.
- [33] G. Lorenzo, T.J.R. Hughes, Dominguez-Frojan P, Reali A, and Gómez H. Computer simulations suggest that prostate enlargement due to benign prostatic hyperplasia mechanically impedes prostate cancer growth. *Proceedings of the National Academy of Sciences*, 116(4):1152–1161, 2019.
- [34] G. Lorenzo, M.A. Scott, K.Tew, T.J.R. Hughes, Y.J. Zhang, L. Liu, G. Vilanova, and H. Gómez. Tissue-scale, personalized modeling and simulation of prostate cancer growth. *Proceedings of the National Academy of Sciences*, 113(48):E7663–E7671, 2016.
- [35] G. Lorenzo, M.A. Scott, K. Tew, T.J.R. Hughes, and H. Gómez. Hierarchically refined and coarsened splines for moving interface problems, with particular application to phase-field models of prostate tumor growth. *Computer Methods in Applied Mechanics and Engineering*, 319:515–548, 2017.

- [36] E. Maggiorcelli. Griffith criterion for steady and unsteady-state crack propagation. In *Mathematical Modeling in Cultural Heritage*, Springer INdAM Series. Springer, (to appear).
- [37] E. Maggiorcelli and M. Negri. Energy release and griffith criterion for phase-field fracture (to appear).
- [38] A. Marengo, A. Patton, M. Negri, U. Perego, and A. Reali. A rigorous and efficient explicit algorithm for irreversibility enforcement in phase-field finite element modeling of brittle crack propagation. *Computer Methods in Applied Mechanics and Engineering*, 387:114137, 2021.
- [39] A. Marengo and U. Perego. A small deformations effective stress model of gradient plasticity phase-field fracture. *Computer Methods in Applied Mechanics and Engineering*, 409:115992, 2023.
- [40] C. Miehe, F. Welschinger, and M. Hofacker. Thermodynamically consistent phase-field models of fracture: variational principles and multi-field FE implementations. *Internat. J. Numer. Methods Engrg.*, 83(10):1273–1311, 2010.
- [41] Sindhu Nagaraja, Ulrich Römer, Hermann G Matthies, and Laura De Lorenzis. Deterministic and stochastic phase-field modeling of anisotropic brittle fracture. *Computer Methods in Applied Mechanics and Engineering*, 408:115960, 2023.
- [42] M. Negri. The anisotropy introduced by the mesh in the finite element approximation of the Mumford-Shah functional. *Numer. Funct. Anal. Optim.*, 20(9-10):957–982, 1999.
- [43] M. Negri. Γ -convergence for high order phase field fracture: continuum and isogeometric formulation. *Comput. Methods Appl. Mech. Engrg.*, 362:112858, 2020.
- [44] K.D. Nguyen, C.-L. Thanh, H. Nguyen-Xuan, and M. Abdel-Wahab. A hybrid phase-field isogeometric analysis to crack propagation in porous functionally graded structures. *Engineering with Computers*, 39:129–149, 2023.
- [45] K. Pham, H. Amor, J.-J. Marigo, and C. Maurini. Gradient damage models and their use to approximate brittle fracture. *International Journal of Damage Mechanics*, 20(4):618–652, 2011.
- [46] L. Piegl and W. Tiller. *The NURBS book*. Springer Science and Business Media, 1996.
- [47] D. Proserpio, M. Ambati, L. De Lorenzis, and J. Kiendl. A framework for efficient isogeometric computations of phase-field brittle fracture in multipatch shell structures. *Computer Methods in Applied Mechanics and Engineering*, 372:113363, 2020.
- [48] D. Proserpio, M. Ambati, L. De Lorenzis, and J. Kiendl. Phase-field simulation of ductile fracture in shell structures. *Computer Methods in Applied Mechanics and Engineering*, 385:114019, 2021.
- [49] F. Vicentini, C. Zolesi, C. Maurini, P. Carrara, and L. De Lorenzis. On the energy decomposition in variational phase-field models for brittle fracture under multi-axial stress states. *Int. J. Fract.*, 247:291–317, 2024.
- [50] T. Wick. *Multiphysics phase-field fracture—modeling, adaptive discretizations, and solvers*, volume 28 of *Radon Series on Computational and Applied Mathematics*. De Gruyter, Berlin, 2020.
- [51] J.-Y. Wu. A unified phase-field theory for the mechanics of damage and quasi-brittle failure. *Journal of the Mechanics and Physics of Solids*, 103:72 – 99, 2017.
- [52] X. Zhuang, S. Zhou, G.D. Huynh, P. Areias, and T. Rabczuk. Phase field modeling and computer implementation: A review. *Engineering Fracture Mechanics*, 262:108234, 2022.